Doctoral Dissertation

Controlling Blood Capillary Structures in Three-Dimensional Tissues by Regulating Elastic Moduli of Scaffolds

尚　玉成

June 2023

Graduate School of Engineering
Osaka University

Content

General Introduction

Tissue engineering (TE) is an interdisciplinary field combining engineering, materials, and biological sciences, which initially focused on the repair or replacement of injured tissues (**Figure 1**). The microenvironment of human tissues generally includes extracellular matrix (ECM), cells, blood capillaries, and lymphatic capillaries.[1] 3D *in vitro* capillary network models began to offer promising solutions for the treatment of a wide range of diseases due to their ability to form complex structures similar to *in vivo* tissues and mimic the physiological environment of natural cellular microvasculature. Their ability to form much more complex structures and their facility to mimic the microenvironment of natural cellular microvasculature.[2,3] Therefore, the *in vitro* construction of 3D capillary network models has become a major focus in the field of tissue engineering, and many such models have been developed for drug testing and toxicity evaluation. The construction of 3D *in vitro* capillary network models is usually influenced by factors such as cell source and type, scaffolds, and mechanical properties.[4–6]

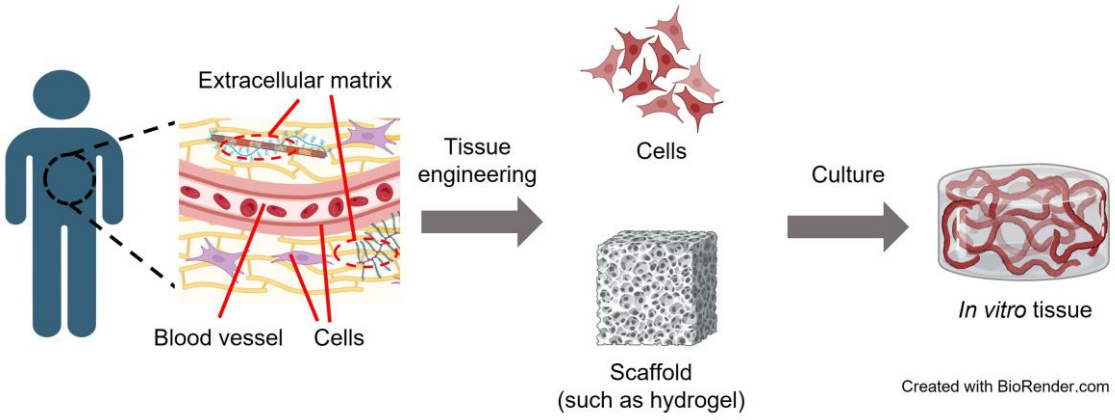

Figure 1. Schematic illustration about construction of 3D *in vitro* tissue.

The *in vitro* construction of blood capillaries for three-dimensional (3D) tissue is important to help mimic the *in vivo* tissue microenvironment. The resultant 3D blood capillary tissue can be used to study the migration of cancer cells in the body and in other areas such as drug testing.[1] Current tissue regeneration scaffolds without a blood capillary network have been generally limited to within 100-200 μm due to the limited diffusion of oxygen and

nutrients which play important roles in the metabolic processes of tissues.[7–9] To develop 3D tissues with a capillary network, it is important to clarify the factors that affect the formation of blood capillaries.

In recent years, various attempts have been made to find more suitable conditions for capillary network construction and these efforts have been mainly focused in two areas.[10] One of these focuses has been on creating interconnected mesopores and microchannels to build a pre-vascularized tissue engineering structure using techniques such as 3D bioprinting, microfluidic devices, electrospinning, molding, and decellularization.[11–17] However, these technologies still have some limitations. For example, 3D bioprinting affects cell viability and the required equipment is expensive.[18,19] Although formation of interconnected perfusable microchannel network using electrospun nonwoven mat has been reported, the diameter of the channels created is usually less than 1 μm, which is markedly smaller than that of normal capillaries (8-10 μm), so it is difficult to integrate endothelial cells.[20] These limit the use of the engineered tissues in high-throughput drug screening. Another way to improve the formation of the blood capillary network is through scaffold culture, cell co-culture, and cell sheet stacking to promote endothelial cell angiogenesis.[21–23]

For the 3D tissue construction, since tissues or organs have a specific range of stiffness, it is necessary to use stiffness adjustable scaffolds to simulate the microenvironment of specific tissues in 3D-model construction (**Figure 2**).[24,25] For example, the construction of a highly distributed capillary network formation of endothelial cells (ECs) in a low-stiffness scaffold has been reported.[26–28] On the other hand, good adhesion and proliferation of ECs on the surface of high stiffness scaffolds has also been reported.[29,30] However, a mechanistic

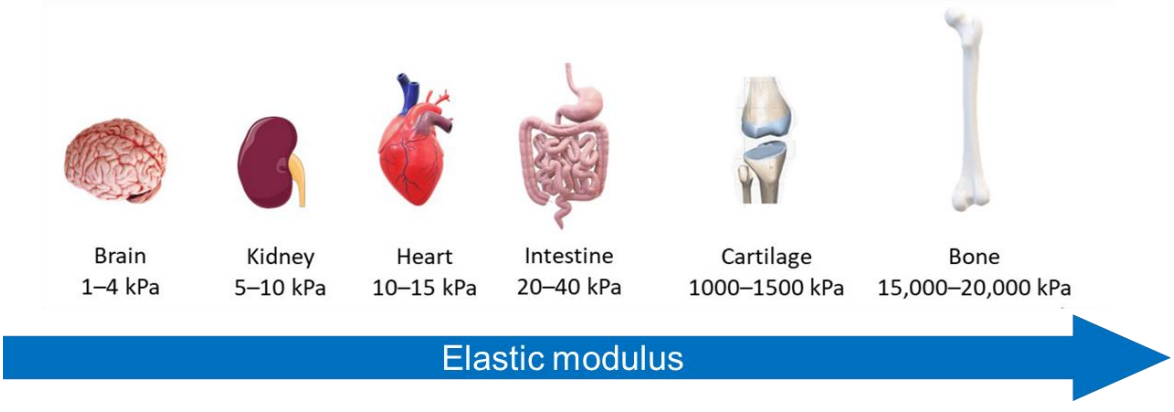

Figure 2. Range of stromal tissue stiffness in human body.

description of the differences in behaviors of ECs in the internal and surface of 3D capillary network models has yet to be elucidated, and the mechanism as shown in **Figure 3**.[31] Generally, for the cell on the scaffold surface, after cell combined with ECM, the cell would secret integrin and make a cluster, in order to induce more integrin, the forces of cytokines is needed to form focal adhesions, then lead cell produce large forces. Finally, the soft scaffold can not afford the forces from cell, make the cell difficult to adhere.

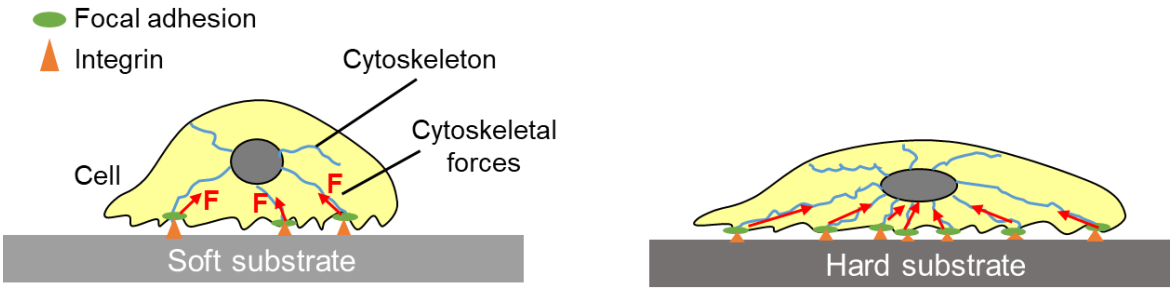

Figure 3. Cell behavior on scaffolds surface with different stiffness

The development of the brain microvascular system is an important part of vascular model construction, which is also known as the blood-brain barrier (BBB) model.[32] The distinguishing feature of the BBB is the selective barrier which protects the brain from external aggression, and separates the peripheral from the central nervous system (CNS).[33,34] During its formation, the BBB is regulated and induced by various growth factors and signaling pathways, such as vascular endothelial growth factor (VEGF), platelet-derived growth factors (PDGF-B and PDGFR-β), typical Wnt signaling, etc.[35,36] The BBB is mainly composed of brain microvascular endothelial cells (BMEC), pericytes (PC), and astrocytes (AC) endfeet. Endothelial cells are interconnected by a junctional complex including tight junctions (TJ) and adherens junctions, surrounded by PCs and ACs, and encapsulated in the basal lamina.[37] BMECs are a type of interconnected and apposition-dependent cells subject to chemical, physical and mechanical stimuli which construct the interface between blood flow and the deformable solid vascular wall.[38] Carriers on BMECs tend to exhibit high-level stereospecificity and participate in the selective transport of small molecules, which are responsible for the BBB properties.[39] PCs are similar to BMECs and are separated by a secreted extracellular matrix (ECM). Their main function is to maintain and regulate the growth of the BBB [40]. The main function of ACs includes synaptic regulation, ion homeostasis, water

homeostasis, and maintenance of cellular pH to maintain BBB behavior.[41,42]

The BBB plays an important role in maintaining brain homeostasis but it is also a major barrier to the delivery of many drugs to the CNS extracellular fluid, and this has limited the development of effective drugs for CNS-related diseases.[43–45] Therefore, it is necessary to develop BBB models to understand its effect in neurological disease pathogenesis and evaluate drug permeability.[46] The BBB has already been constructed by implementing various microfabrication and microfluidic techniques. The Transwell model consists of two compartments physically separated by a porous membrane, and the BBB is usually formed by co-culture of a BMEC monolayer (upper compartment) with ACs and/or PCs (lower compartment), immersed in an in vivo-like microenvironment of permeable membranes.[47–49] The Transwell model is the most common BBB model and is considered to be low-cost, reproducible and easy to evaluate.[50] However, cells in the Transwell model are not exposed to a flow environment and therefore lack the effect of shear stress on endothelial cell differentiation.[51,52] In addition, the two-dimensional morphology of the Transwell model cannot replicate the structure of brain vessels or capillaries, meaning it lacks some important BBB characteristics.[53,54] Elsewhere, some dynamic models have been developed, such as microfluidic chips. The main goal of these models is to simulate the real dynamic microenvironment of the BBB, thus overcoming some of the limitations of the Transwell model.[32] Simulated blood flow generates shear stress at the lumen surface of the BBB. In fact, shear-induced friction activates many mechanotransduction pathways, known to be important for cell differentiation and tight junction formation.[55,56] However, the dynamic modeling approach also had many limitations. First, these models are much more complex to build than the Transwell model, requiring special equipment as well as higher cost.[57] In addition, the thickness of the wall separating BMECs from ACs is too thick (>100 μm), which is not conducive to simulating a significant reduction in compound by pass transport.[58,59] In general, *in vitro* BBB models that can be easily regulated are still required.

From above information, we found most of them focus on functional studies of the BBB in order to be used for assessing the permeability of drugs.[43–45] However, the mechanical properties of the ECM also influence the behavior of cells in the BBB and the formation of

vascular networks, but few report that ECM stiffness affecting BBB model function, and only the effect of substrate on BBB function in 2D culture has been reported.[60] Therefore, it is necessary to construct a 3D BBB *in vitro* model and investigate the relationship between matrix stiffness and BBB formation.[61]

In this thesis, the author aimed to control the capillary formation by using mechanobiology. First, a high-throughput 3D capillary network model was fabricated by sedimentary culture method. Afterwards, capillary formation was regulated by adjusting the density of scaffold material and cells. Then, introduced a unique method of controlling the blood capillary networks and characteristic holes formation in a BBB model by varying the elastic modulus of a 3D scaffold. Then, the relationship between enzymatic degradation of the scaffolds and capillary hole formation was evaluated. Finally, based on the findings obtained from previous results, hydrogel with opening hole structures was fabricated by using a collagenase solution that mimics the metalloproteinase secreted by endothelial cells. Furthermore, the effect of the volume and incubation time of the collagenase solution on the hole structure formation was also evaluated.

Outline of this thesis

In this thesis, the author describes the methods to control the capillary network and hole structure formation by regulating elastic modulus of scaffolds in 3D tissues.

Chapter 1

Effect of Extracellular Matrix and Cell Density on Blood Capillary Formation in Three-dimensional Tissue

In chapter 1, to improve the vascularization of 3D tissue, elements including growth factors and scaffold type have been found to affect the construction of 3D capillary structures. However, the effect of the other factors such as modulus or cell number on blood capillary remain unclear. In this work, a 3D-human blood capillary model was fabricated via sedimentary culture method, based on 3D culture of endothelial cells (HUVEC) and fibroblasts (NHDF) with the support of collagen microfibers (CMFs) as an extracellular matrix. The amount of CMF or cell number was varied to evaluate the relationship between tissue modulus and blood capillary length.

Chapter 2

Control of capillary networks and hole structures by regulating elastic modulus of scaffolds in 3D Blood-Brain Barrier models

In chapter 2, we wanted to clarify the mechanism of mechanical strength of scaffolds on capillary network formation. Therefore, scaffold materials with adjustable mechanical strength were required. We have previously reported the construction of an in vitro BBB capillary network model based on fibrin gels. The model has capillary opening holes on the bottom and thus exhibits perfusable properties. However, the mechanism of hole structure formation in this model has not been entirely clarified, and we have not identified if the capillary network structure could be regulated by changing the scaffold's mechanical properties.

Chapter 3

Construction of enzyme digested holes on hydrogel surface inspired by cell migration

behavior

Previously, we discovered a novel phenomenon of hole formation by endothelial cells migration on the surface of fibrin gels. Interestingly, the hole formation, such as depth and number, was significantly influenced by the gel stiffness, but the detail of the hole formation was not clarified yet. In this chapter 3, we tried to understand the effect of hydrogel stiffness on the hole formation by dropping collagenase solution onto the surface of the hydrogels because the endothelial cells migration was performed by metalloproteinases digestion.

Reference

[1] D. Hikimoto, A. Nishiguchi, M. Matsusaki, M. Akashi, *Adv. Healthcare Mater.* **2016**, *5*, 1969.

[2] F. Pampaloni, E. G. Reynaud, E. H. K. Stelzer, *Nat Rev Mol Cell Biol* **2007**, *8*, 839.

[3] G. A. Truskey, *F1000Res* **2016**, *5*, 1045.

[4] D. Hielscher, C. Kaebisch, B. J. V. Braun, K. Gray, E. Tobiasch, *Stem Cell Rev and Rep* **2018**, *14*, 642.

[5] C. D. Devillard, C. A. Marquette, *Front. Bioeng. Biotechnol.* **2021**, *9*, 721843.

[6] S. T. Lust, C. M. Shanahan, R. J. Shipley, P. Lamata, E. Gentleman, *Acta Biomaterialia* **2021**, *132*, 114.

[7] J. Liu, J. Hilderink, T. A. M. Groothuis, C. Otto, C. A. van Blitterswijk, J. de Boer, *J Tissue Eng Regen Med* **2015**, *9*, 952.

[8] H. Gaskell, P. Sharma, H. E. Colley, C. Murdoch, D. P. Williams, S. D. Webb, *Toxicol. Res.* **2016**, *5*, 1053.

[9] L. De Moor, I. Merovci, S. Baetens, J. Verstraeten, P. Kowalska, D. V. Krysko, W. H. De Vos, H. Declercq, *Biofabrication* **2018**, *10*, 035009.

[10] Z. Wang, S. M. Mithieux, A. S. Weiss, *Adv. Healthcare Mater.* **2019**, *8*, 1900742.

[11] H. Liu, S. Kitano, S. Irie, R. Levato, M. Matsusaki, *Adv. Biosys.* **2020**, *4*, 2000038.

[12] L. Ouyang, J. P. K. Armstrong, Q. Chen, Y. Lin, M. M. Stevens, *Adv. Funct. Mater.* **2020**, *30*, 1908349.

[13] S. Kim, H. Lee, M. Chung, N. L. Jeon, *Lab Chip* **2013**, *13*, 1489.

[14] Y. Nashimoto, T. Hayashi, I. Kunita, A. Nakamasu, Y. Torisawa, M. Nakayama, H. Takigawa-Imamura, H. Kotera, K. Nishiyama, T. Miura, R. Yokokawa, *Integr. Biol.* **2017**, *9*, 506.

[15] J. B. Lee, X. Wang, S. Faley, B. Baer, D. A. Balikov, H.-J. Sung, L. M. Bellan, *Adv. Healthcare Mater.* **2016**, *5*, 781.

[16] A. Tocchio, M. Tamplenizza, F. Martello, I. Gerges, E. Rossi, S. Argentiere, S. Rodighiero, W. Zhao, P. Milani, C. Lenardi, *Biomaterials* **2015**, *45*, 124.

[17] S. Pashneh-Tala, S. MacNeil, F. Claeyssens, *Tissue Engineering Part B: Reviews* **2016**, *22*, 68.

[18] W. Liu, Z. Zhong, N. Hu, Y. Zhou, L. Maggio, A. K. Miri, A. Fragasso, X. Jin, A. Khademhosseini, Y. S. Zhang, *Biofabrication* **2018**, *10*, 024102.

[19] W. Jia, P. S. Gungor-Ozkerim, Y. S. Zhang, K. Yue, K. Zhu, W. Liu, Q. Pi, B. Byambaa, M. R. Dokmeci, S. R. Shin, A. Khademhosseini, *Biomaterials* **2016**, *106*, 58.

[20] C. Gualandi, A. Zucchelli, M. Fernández Osorio, J. Belcari, M. L. Focarete, *Nano Lett.* **2013**, *13*, 5385.

[21] B. A. Juliar, J. A. Beamish, M. E. Busch, D. S. Cleveland, L. Nimmagadda, A. J. Putnam, *Biomaterials* **2020**, *230*, 119634.

[22] Y.-M. Kook, Y. Jeong, K. Lee, W.-G. Koh, *J Tissue Eng* **2017**, *8*, 204173141772464.

[23] N. Asakawa, T. Shimizu, Y. Tsuda, S. Sekiya, T. Sasagawa, M. Yamato, F. Fukai, T. Okano, *Biomaterials* **2010**, *31*, 3903.

[24] D. Baruffaldi, G. Palmara, C. Pirri, F. Frascella, *ACS Appl. Bio Mater.* **2021**, *4*, 2233.

[25] F. Carotenuto, S. Politi, A. Ul Haq, F. De Matteis, E. Tamburri, M. L. Terranova, L.

Teodori, A. Pasquo, P. Di Nardo, *Micromachines* **2022**, *13*, 780.
[26] M. Vigen, J. Ceccarelli, A. J. Putnam, *Macromol. Biosci.* **2014**, *14*, 1368.
[27] A. Brown, H. He, E. Trumper, J. Valdez, P. Hammond, L. G. Griffith, *Biomaterials* **2020**, *243*, 119921.
[28] K. Chwalek, M. V. Tsurkan, U. Freudenberg, C. Werner, *Sci Rep* **2014**, *4*, 4414.
[29] Y. Guo, F. Mei, Y. Huang, S. Ma, Y. Wei, X. Zhang, M. Xu, Y. He, B. C. Heng, L. Chen, X. Deng, *Bioactive Materials* **2022**, *7*, 364.
[30] Y.-T. Yeh, S. S. Hur, J. Chang, K.-C. Wang, J.-J. Chiu, Y.-S. Li, S. Chien, *PLoS ONE* **2012**, *7*, e46889.
[31] F. J. Alenghat, D. E. Ingber, *Sci. STKE* **2002**, *2002*, DOI 10.1126/stke.2002.119.pe6.
[32] A. Aazmi, H. Zhou, W. Lv, M. Yu, X. Xu, H. Yang, Y. S. Zhang, L. Ma, *iScience* **2022**, *25*, 104110.
[33] N. J. Abbott, *Cell Mol Neurobiol* **2005**, *25*, 5.
[34] M. Campisi, Y. Shin, T. Osaki, C. Hajal, V. Chiono, R. D. Kamm, *Biomaterials* **2018**, *180*, 117.
[35] H.-C. Bauer, I. A. Krizbai, H. Bauer, A. Traweger, *Front. Neurosci.* **2014**, *8*, DOI 10.3389/fnins.2014.00392.
[36] M. D. Sweeney, Z. Zhao, A. Montagne, A. R. Nelson, B. V. Zlokovic, *Physiological Reviews* **2019**, *99*, 21.
[37] Y. Serlin, I. Shelef, B. Knyazer, A. Friedman, *Seminars in Cell & Developmental Biology* **2015**, *38*, 2.
[38] Q. Yu, H. Tao, X. Wang, M. Li, *Neural Regen Res* **2015**, *10*, 1882.
[39] B. Engelhardt, H. Wolburg, *Eur. J. Immunol.* **2004**, *34*, 2955.
[40] L. S. Brown, C. G. Foster, J.-M. Courtney, N. E. King, D. W. Howells, B. A. Sutherland, *Front. Cell. Neurosci.* **2019**, *13*, 282.
[41] I. Matias, J. Morgado, F. C. A. Gomes, *Front. Aging Neurosci.* **2019**, *11*, 59.
[42] S. J. Miller, *Front. Cell. Neurosci.* **2018**, *12*, 401.
[43] W. M. Pardridge, *Molecular Interventions* **2003**, *3*, 90.
[44] W. M. Pardridge, *Drug Discovery Today* **2002**, *7*, 5.
[45] N. J. Abbott, *J Inherit Metab Dis* **2013**, *36*, 437.
[46] M. Piantino, D.-H. Kang, T. Furihata, N. Nakatani, K. Kitamura, Y. Shigemoto-Mogami, K. Sato, M. Matsusaki, *Materials Today Bio* **2022**, *15*, 100324.
[47] K. Hatherell, P.-O. Couraud, I. A. Romero, B. Weksler, G. J. Pilkington, *Journal of Neuroscience Methods* **2011**, *199*, 223.
[48] S. Santaguida, D. Janigro, M. Hossain, E. Oby, E. Rapp, L. Cucullo, *Brain Research* **2006**, *1109*, 1.
[49] G. Linz, S. Djeljadini, L. Steinbeck, G. Köse, F. Kiessling, M. Wessling, *Biosensors and Bioelectronics* **2020**, *165*, 112345.
[50] A. Williams-Medina, M. Deblock, D. Janigro, *Front. Med. Technol.* **2021**, *2*, 623950.
[51] P. Naik, L. Cucullo, *Journal of Pharmaceutical Sciences* **2012**, *101*, 1337.
[52] G. D. Vatine, R. Barrile, M. J. Workman, S. Sances, B. K. Barriga, M. Rahnama, S. Barthakur, M. Kasendra, C. Lucchesi, J. Kerns, N. Wen, W. R. Spivia, Z. Chen, J. Van Eyk, C. N. Svendsen, *Cell Stem Cell* **2019**, *24*, 995.
[53] M. W. van der Helm, A. D. van der Meer, J. C. T. Eijkel, A. van den Berg, L. I. Segerink,

Tissue Barriers **2016**, *4*, e1142493.
[54] M. D. Sweeney, S. Ayyadurai, B. V. Zlokovic, *Nat Neurosci* **2016**, *19*, 771.
[55] M. Raasch, K. Rennert, T. Jahn, C. Gärtner, G. Schönfelder, O. Huber, A. E. M. Seiler, A. S. Mosig, *Biomicrofluidics* **2016**, *10*, 044102.
[56] M. Piantino, A. Figarol, M. Matsusaki, *Front. Toxicol.* **2021**, *3*, 656254.
[57] N. R. Wevers, D. G. Kasi, T. Gray, K. J. Wilschut, B. Smith, R. van Vught, F. Shimizu, Y. Sano, T. Kanda, G. Marsh, S. J. Trietsch, P. Vulto, H. L. Lanz, B. Obermeier, *Fluids Barriers CNS* **2018**, *15*, 23.
[58] S. Bang, S.-R. Lee, J. Ko, K. Son, D. Tahk, J. Ahn, C. Im, N. L. Jeon, *Sci Rep* **2017**, *7*, 8083.
[59] C. Kulczar, K. E. Lubin, S. Lefebvre, D. W. Miller, G. T. Knipp, *Journal of Pharmacy and Pharmacology* **2017**, *69*, 1684.
[60] A. M. Bosworth, H. Kim, K. P. O'Grady, I. Richter, L. Lee, B. J. O'Grady, E. S. Lippmann, *Cel. Mol. Bioeng.* **2022**, *15*, 31.
[61] F. Du, E. V. Shusta, S. P. Palecek, *Front. Chem. Eng.* **2023**, *5*, 1130127.

Chapter 1

Effect of Extracellular Matrix and Cell Density on Blood Capillary Formation in Three-Dimensional Tissue

1.1 Introduction

The construction of three-dimensional (3D) capillary tissue is still a central issue in the field of tissue engineering. To improve the vascularization of 3D tissue, elements including growth factors and scaffold type have been found to affect the construction of 3D capillary structures. However, the effect of the other factors such as modulus or cell number on blood capillary remain unclear.

Previous studies have reported that an increase in cell space in the tissue will weaken the interaction between cells.[1] Therefore, on the premise of ensuring that the amount of collagen, which has been reported in our previous studies to promote cell adhesion, blood capillary alignment, and mechanical property of the 3D tissues, is sufficient as a scaffold. It is speculated that by maintaining the cell number, a denser ECM tissue structure can be fabricated by increasing the amount of CMF.[6] Its elastic modulus will increase as a consequence, but it will also cause the interaction between cells to decrease, negatively affecting capillary growth.

We recently reported a unique approach called ‘sedimentary culture’ using CMF to fabricate large-scale engineered tissues.[2–4] Via the blending and co-culture of CMF, normal human dermal fibroblasts (NHDF) and human umbilical vein endothelial cells (HUVEC), millimeter-level wholly-vascularized engineered tissue with high ECM density were obtained. Nevertheless, it is still unclear what factors, such as the elastic modulus of ECM formed by CMF or the number of fibroblasts or endothelial cells, affect the growth of capillaries. Based on previous research, we fabricated 3D blood capillary tissue and evaluated the effects of the aforementioned variables on capillary growth by regulating the amount of CMF and the number of cells in this chapter. The elucidation of these mechanisms will make it easier to obtain high-throughput well-grown capillary 3D tissue in the future.

1.2 Experiments

1.2.1 Materials

Porcine skin collagen type I powder was purchased from Nippi, Inc. (Tokyo, Japan). The 24-well cell culture insert with a 0.4 μm pore size was purchased from Corning (NY, U.S.A.), while 6- and 24-well cell culture plates were purchased from Iwaki (Tokyo, Japan). Normal human dermal fibroblasts (NHDF, CC-2509) were cultured in Dulbecco's modified Eagle medium (DMEM High-Glucose, Nacalai Tesque, 08458) with 10% fetal bovine serum (FBS, 35010163, Corning, NY, USA) and 1% antibiotic (02892-54, Nacalai Tesque, Kyoto, Japan). Human umbilical vein endothelial cells (HUVEC: C25271) were cultured in KBM VEC-1 (KOHJIN BIO, 16030100). Goat anti-mouse secondary antibody (Alexa Fluor 647, A21235) and 4′,6-diamidino-2-phenylindole (DAPI) were obtained from Thermo Fisher Scientific (MA, USA). DNeasy Blood Tissue kit (250) (160042377) was purchased from Qiagen (Tokyo, Japan). 4%-paraformaldehyde (PFA, Wako, 30525-89-4) and monoclonal mouse anti-human CD31 antibody (DAKO, #M0823) were used without further purification. Bovine serum albumin (BSA, A3294), phosphate-buffered saline powder (PBS, D5652), and Triton-X 100 (T8787) were purchased from Sigma-Aldrich (MO, USA).

1.2.2 Preparation of Collagen Microfibers

The porcine skin collagen type I powder (Nippi, Inc., Tokyo, Japan) was irradiated under UV light for 1 minute to kill possible bacteria or fungi, then mixed with PBS solution and homogenized for 1 min at 30,000 rpm (Violamo VH-10 homogenizer AS ONE, Osaka, Japan, S10N-10G with 10 mm diameter and 115 mm length probe). The CMF suspension was then divided into microtubes and centrifuged (Kubota 3520, Tokyo, Japan) at 10,000 rpm for 1 min and the supernatant was aspirated.

The lengths of CMF in PBS were measured from phase-contrast images produced by

optical microscopy. The characterizations of CMF were analyzed by circular dichroism (CD) spectrum and sodium dodecyl sulfate-polyacrylamide gel electrophoresis (SDS-PAGE) to check the triple helix structure and molecular weight. CD spectra were obtained using a CD spectrometer (JASCO model PTC-348WI, J-1500, Tokyo, Japan). The samples (0.05 mg mL^{-1}) were prepared in acetic acid (50×10^{-3} M) in a quartz cell. Spectra were recorded from 200 to 250 nm with 0.5 nm increments at a scanning rate of 100 nm min^{-1}. The raw CD signal was normalized by the concentration and by the number of residues.

For SDS-PAGE, samples (0.5 wt%) were diluted in running buffer for SDS-Tris-Glycine (DCB-423468, Cosmo Bio Co. Ltd.). Samples were then mixed with β-ME sample treatment (DCB-423437, Cosmo Bio Co. Ltd.) for denaturation. Next, samples were heated at 90 °C for 5 min and then 5 μL of protein marker (SIMASIMA Prestained Broad Range Protein, DCB-SS2000-3, Cosmo Bio Co. Ltd.) and 10 μL of the sample were loaded onto a polyacrylamide gel in the running buffer. Electrophoresis was performed at 20 mA per gel for 1 h. Samples in the gel were then stained with Page Blue 83 Stain Reagent (CBB-R250) (DCB-423406, Cosmo Bio Co. Ltd.) for 1 hour and subsequently de-stained in a solution containing water (87.5%), methanol (5%), and acetic acid (7.5%). The molecular weight of each band of collagen was visualized on a Bio-Rad ChemiDoc™ MP Imaging System.

1.2.3 Fabrication of 3D-Blood Capillary Models Using CMF

The experiment can be divided into two parts: A fixed cell amount condition and a fixed CMF amount condition. In the first, the desired CMF amount (3, 5, 7, 10 mg) was mixed with only medium, 1×10^6 NHDF, or 1×10^6 NHDF and 1×10^6 HUVEC homogeneously. In the second, the fixed CMF amount (3 mg) was mixed with NHDF (0, 1×10^5, 5×10^5, 1×10^6, 5×10^6, 1×10^7) and HUVEC (5×10^5), or mixed with NHDF (0, 1×10^5, 5×10^5, 1×10^6, 5×10^6) and HUVEC (1×10^6), or mixed with NHDF (1×10^6) and HUVEC (0, 1×10^5, 1×10^6, 2×10^6, 5×10^6). They were then seeded in 24-well cell culture inserts and centrifuged for 15 min at 1,100 g, RT, respectively. Finally, inserts were assembled into 6-well plates filled with 12 mL medium to ensure that the inserts were completely immersed. The 3D tissues were then incubated in 5%

CO_2 at 37 °C for 1 week in the mix culture medium (50% DMEM : 50% KBM VEC-1), and the medium was changed every 3 or 4 days.

1.2.4 Fluorescence Imaging and Histological Analysis

The nuclei were stained with DAPI and HUVEC were detected by the anti-CD31 antibody. Specifically, the tissues were fixed in 4% paraformaldehyde (2 hours, room temperature), then permeabilized with 0.02% Triton X-100 (10 min) and blocked with 1 wt% BSA (1×PBS, 25 min). The tissues were then incubated with primary antibodies (anti-CD31 antibody, diluted at 1/50 in 1×PBS) for 1.5 hours. After washing the tissues 3 times by 1×PBS, the secondary antibodies (goat-anti mouse, Alexa Fluor 647, DAPI, 1:100 dilution in 1×PBS) were incubated for 1 hour. After washing in the 1×PBS, the 3D tissue was finally observed using a confocal laser scanning microscope (CLSM) (Confocal Quantitative Image Cytometer CQ1, Yokogawa, Japan). For histology staining, the fixed 3D tissues were immersed into PBS and sent to the Applied Research Company for paraffin embedding. Sectioned 3D tissues were stained with hematoxylin-eosin (HE) or CD31 (Abcam, ab182981) staining. The images were captured using an FL EVOS Auto microscope (Thermo Fisher). Analyses of the fluorescence and histological images were conducted using ImageJ Fiji software for 3D tissue capillary length.

1.2.5 Mechanical Elastic Modulus Measurements

After one week of culture, the 3D tissues were removed from the medium and prepared for compression test. Compression experiments were conducted to explore the mechanical behaviors under a 1 N loading cell by a 5 mm spherical indenter using an EZ-TEST instrument (Shimadzu, Kyoto, Japan) at a 1 mm min^{-1} loading speed. To eliminate any interference during the indention, only the stable range of 5-10% stress in the stress-strain curve was considered and further fitted into a linear slope. Young's modulus of elasticity was automatically calculated by the instrument's own software.

1.2.6 Statistical analysis

All data are expressed as means ± SD, unless otherwise specified. The values represent the means ± SD from three independent experiments. Statistical comparisons between groups were analyzed using two-tailed Student's t-tests. Values <0.05 were considered to be statistically significant. These are indicated in the graphs as $*p < 0.05$, $**p < 0.01$. N.D. denotes no data.

1.3 Results and discussion

1.3.1 Characterization of CMF

After homogenization of the collagen powder, the average length of the obtained CMF was measured from the phase contrast (Ph) image (**Figure 1-1a**). The calculated value was 28.3 ± 7.9 μm **(Figure 1-1b**), confirming that the CMF have good homogeneity and dispersion. In addition, CMF with a size of about 20 μm have been confirmed in previous reports to show a similar sedimentation velocity with cells, which is conducive to the uniform distribution of cells in the manufacture of 3D capillary tissue.[5,6] In the homogenization process, the high temperature caused by the high speed of the homogenizer may cause the denaturation of CMF, so CD spectral analysis was performed. The results of this analysis depicted in **Figure 1-1c** showed a characteristic peak near 220 nm, which is a typical triple supercoil structure, similar

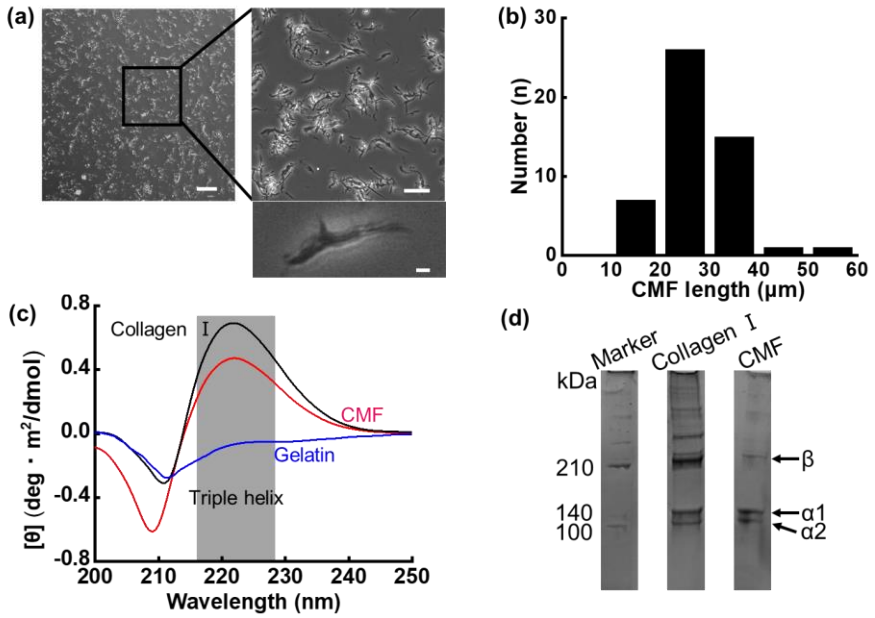

Figure 1-1. (a) Phase-contrast image of collagen microfiber (CMF) at different magnifications. Scale bars are 200 μm (left), 50 μm (middle), and 5 μm (right). (b) Fiber length distribution of CMF calculated from Ph images in (a) (n = 50), indicates that CMF has high uniformity. (c) Circular dichroism (CD) spectrum of CMF to demonstrate that its helical structure was maintained after homogenization treatment. CMF was compared with collagen type I and gelatin for CD measurement. (d) The SDS-PAGE measurement to show the retained molecular weight of CMF after homogenization treatment. CMF was compared with collagen I for SDS-PAGE.

to the natural Col I in the control group and did not appear here in the gelatin control. In addition, the negative peaks near 205-210 nm are also present in the both collagen spectrum and due to the random coil in collagen structure, indicates that the natural Col I character of CMF remained.[7–9] Meanwhile, CMF molecules and Col I molecules were also analyzed by sodium dodecyl sulfate-polyacrylamide gel electrophoresis (SDS-PAGE), showing the typical pattern of type I collagen chains (**Figure 1-1d**), with bands at 210 kDa (β), 130 kDa (α1), and 120 kDa (α2) molecular weights. Therefore, the above results indicate that the homogenized CMF did not undergo denaturation.

1.3.2 Effects of varying CMF amount on the elastic modulus of tissues

To evaluate the effect of varying CMF amount on the elastic modulus of tissue, the tissues cultured for 7 days were subjected to a compression test (**Figure 1-2**). There were three types of test subjects: only CMF (red color); CMF and NHDF (orange color); CMF, NHDF, and HUVEC (blue color), where the number of NHDF were fixed at 1×10^6 cells, and the number of HUVEC were fixed at 5×10^5 cells. Interestingly, the results of the experiment were quite different from what we expected in that, the modulus of the tissue did not increase with an increased amount of CMF. In the control group (only CMF), the modulus of the tissue hardly changed with an increase in the amount of CMF. In the other two groups, the modulus of the tissue decreased as the amount of CMF increased. We hypothesize that the NHDF in the CMF scaffold can secrete collagen as a cross-linking agent

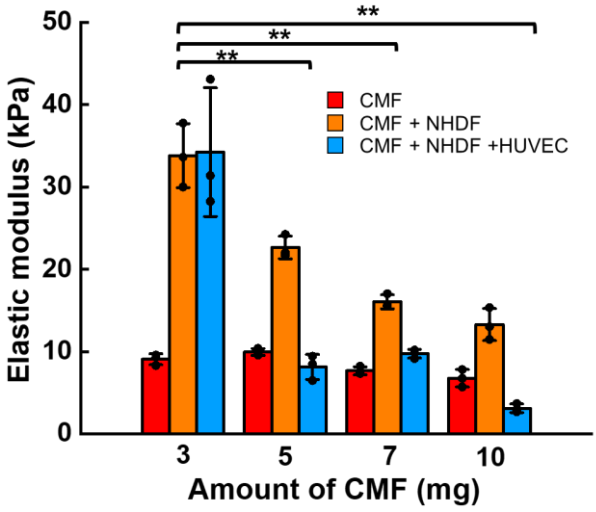

Figure 1-2. Compression test to measure the elastic modulus of 3D tissue. The color red are CMF-only samples, orange are CMF with NHDF cells samples (**$p < 0.01$), blue are CMF with HUVECs and NHDF cells (**$p < 0.01$), all samples n=3. The elastic modulus is hardly affected by the amount of CMF.

to strengthen the tissue structure. Therefore, in the orange and blue groups, increasing the amount of CMF will reduce the density of NHDF in the 3D tissue due to the increased total tissue volume, which in turn leads to the secreted collagen not being sufficient to support the structure of the tissue, ultimately decreasing its mechanical strength. For the blue group, excessively thick tissue will make the cells in the deep layer hypoxic, affect the migration and proliferation of HUVEC, and may cause the collapse of the tissue structure and the decrease of mechanical strength. In addition, the 3D capillary tissue model after one week of culture was also fixed and immunostained with CD31 antibody (a specific marker of endothelial cells). Then observed by CLSM, as shown in **Figure 1-3(a-d)**, the existence of a blood capillary network in the 3D tissue model was confirmed, and the image was skeletonized using ImageJ software. Five equal areas were selected, and then the average length and total length of the capillaries were measured. Here, the capillary length is defined as the distance between two junctions of capillary branches. With the increase of CMF amount, both the average and total capillary lengths showed a gradually decreasing trend. Therefore, a fixed amount of 3 mg CMF was selected for subsequent experiments.

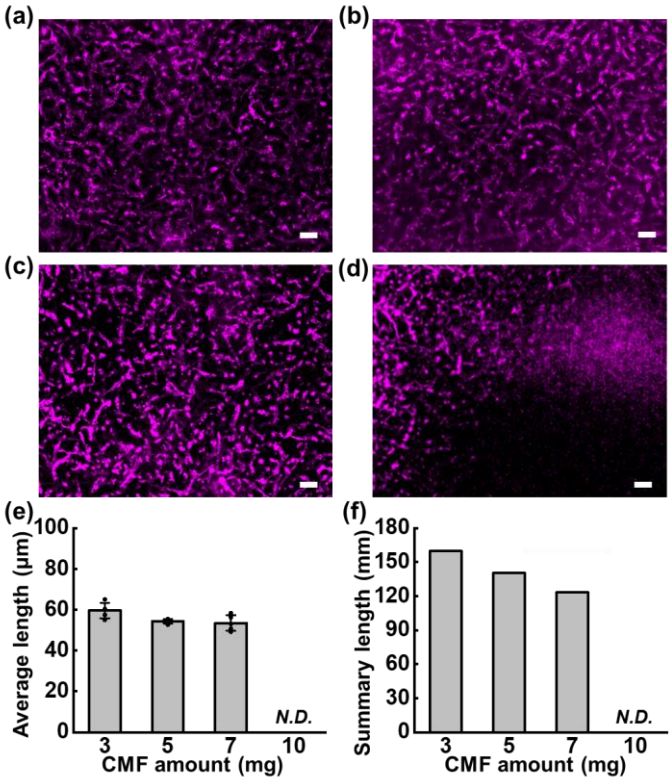

Figure 1-3. (a-d) The observation of blood capillary by CD31 immunostaining under CQ1, all of the samples have same HUVEC number (5×10^5) and same NHDF number (1×10^6), scale bar = 100 μm (e-f) The total and average length in a fixed area of 3D capillary structure calculated by ImageJ (n=5).

1.3.3 The effect of NHDF number on tissue mechanical strength and blood capillary growth

First, using the same amount of CMF (3 mg) and HUVEC number (5×10^5), the experiment was carried out by adjusting the number of NHDF (0, 1×10^5, 5×10^5, 1×10^6, 5×10^6, 1×10^7). The 3D capillary tissue model after one week of culture was also fixed and immunostained with CD31 antibody. Then observed by CLSM, as shown in **Figure 1-4a**, only samples with clear

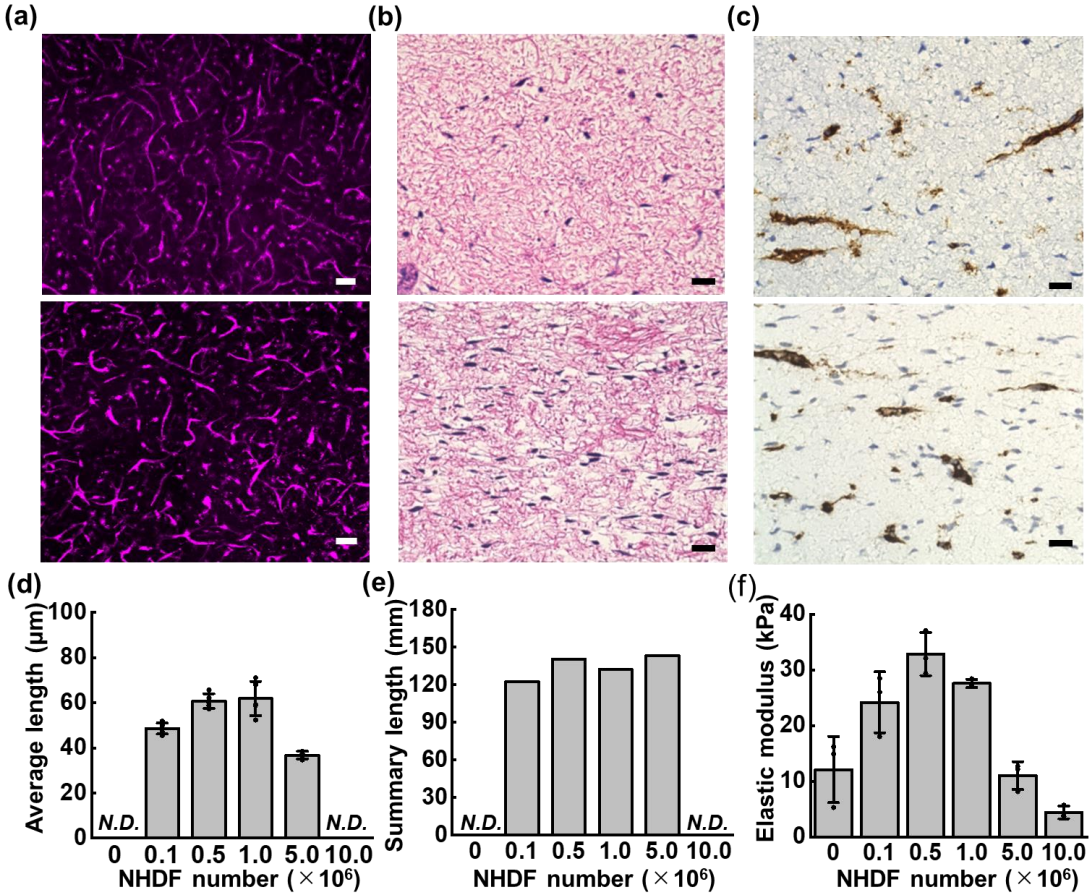

Figure 1-4. (a) Observation of blood capillary by CD31 immunostaining under CLSM. All of the samples have the same HUVECs number (5×10^5), the NHDFs number are 5×10^5 (above), 1×10^6 (below), scale bar = 100 μm, samples are the same in (b) and (c). (b) Histological evaluation of constructed 3D capillary tissues with various differentiation NHDF amounts. Samples are assigned to hematoxylin-eosin stain, purple and pink indicate HUVEC and NHDF nuclei and extracellular matrix, respectively, scale bar = 20 μm. (c) are assigned to anti-CD31 stain antibody, brown suggests the formation of capillary. Scale bar = 20 μm. (d-e) The average and total length in a fixed area of 3D capillary structure was calculated by ImageJ (n=5). (f) The stiffness of different 3D capillary tissue, the NHDFs number are 0 from 1×10^7.

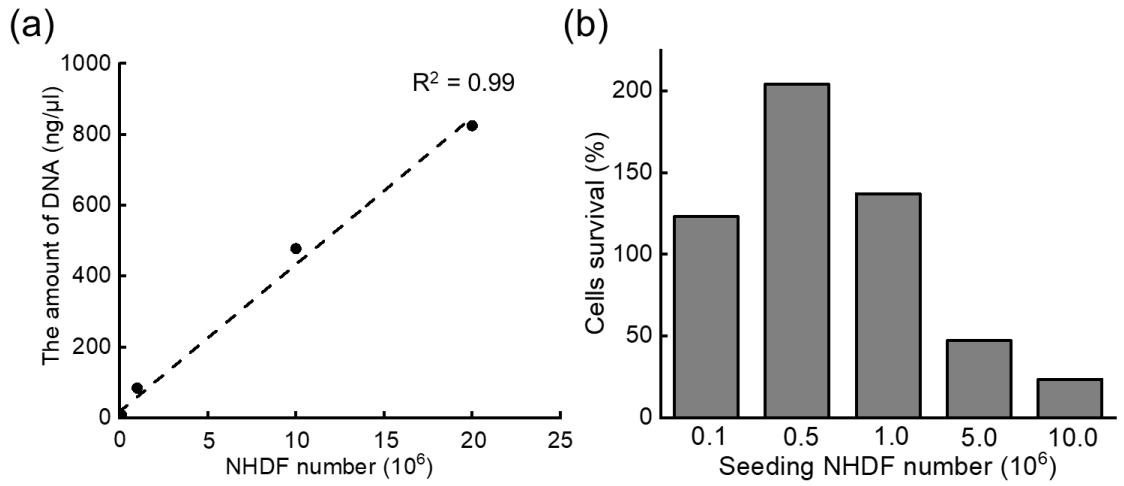

Figure 1-5. (a) Standard curve of the relationship between NHDF number with DNA amount inside the NHDF cells. The DNA amount measured by DNA assay kit. (b) Cells survival rate calculation of the 3D capillary tissue after 7 days culture, all the samples have same HUVECs number (5×10^5).

blood capillary images were selected for display (NHDF-5×10^5, NHDF-1×10^6). After fluorescence staining observation and histological evaluation (**Figure 1-4(b-c)**), the existence of a blood capillary network in the 3D tissue model was also confirmed, and the image was skeletonized using ImageJ software. Five equal areas were also selected, and then the average length (**Figure 1-4d**) and total length of the capillaries were measured (**Figure 1-4e**). Among these samples, no capillary structure was observed in NHDF-0 and NHDF-1×10^7. As shown in the graph, as the number of NHDF increased, the average capillary length in all tissue models increased first and then decreased. The NHDF-5×10^5 and NHDF-1×10^6 samples had the longest average capillary length. Once too much NHDF was added, the average length of capillaries decreased sharply. However, the total capillary length of each sample was almost the same. The stiffness of all samples was tested (**Figure 1-4f**), and it was found that the elastic modulus of the tissues also showed a trend of first increasing and then decreasing with the increase of NHDF number. Therefore, it is predicted that when a large number of NHDFs are added into the construction of the tissue model, it will cause a lack of oxygen and nutrients, which will lead to the death of a large number of cells in the tissue, and the growth of capillaries will also be inhibited. Dead cells also cause the collapse of tissue structure. Therefore, the mechanical strength of the tissue would be reduced.

To confirm this hypothesis, we calculated the cell survival rate of the cultured tissue. First,

the standard curves of NHDF quantity and DNA content in NHDF were calculated (**Figure 1-5a**). We then measured the DNA content in the tissue after one week of culture. The number of viable NHDF in the tissue could be calculated by the standard curve, and the ratio of it to the number of NHDF initially seeded was the survival rate of NHDF. As shown in **Figure 1-5b**, as the number of introduced NHDF increased, the survival rate of NHDF in the tissues cultured for one week generally declined, which was consistent with our previous conjecture.

1.3.4 The effect of HUVEC number on tissue mechanical strength and blood capillary growth

Compared with the previous experiment, the number of HUVEC was slightly increased to 1×10^6, and the amount of CMF was maintained at 3 mg. As a control, the number of NHDF was kept constant (0, 1×10^5, 5×10^5, 1×10^6, 5×10^6). As shown in **Figure 1-6(a-c)**, fluorescence images of CD31 antibody immunostaining were taken by CLSM, and the average length and total length of capillaries of each sample were calculated (**Figure 1-6(d-e)**). Similarly, the elastic modulus of each sample was also measured (**Figure 1-6f**). In line with the previous

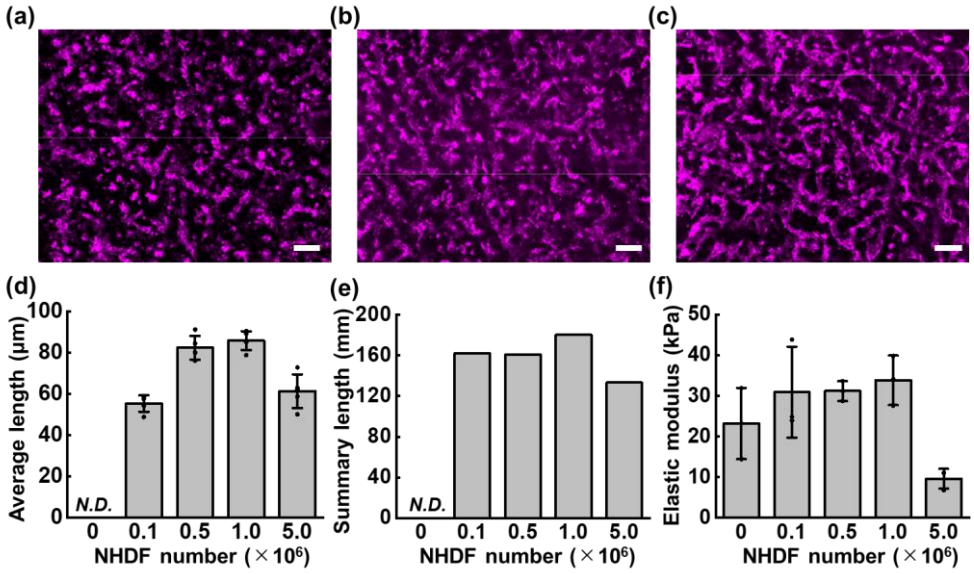

Figure 1-6. (a-c) Observation of blood capillary by CD31 immunostaining under CLSM. All of the samples have the same HUVECs number (1×10^6), the NHDFs number is 1×10^5 (a), 5×10^5 (b), 1×10^6 (c), scale bar = 100 μm, (d-e) The total and average length in a fixed area of 3D capillary structure calculated by ImageJ (n=5). (f) The stiffness of different 3D capillary tissue, the NHDFs number are 0 from 5×10^6.

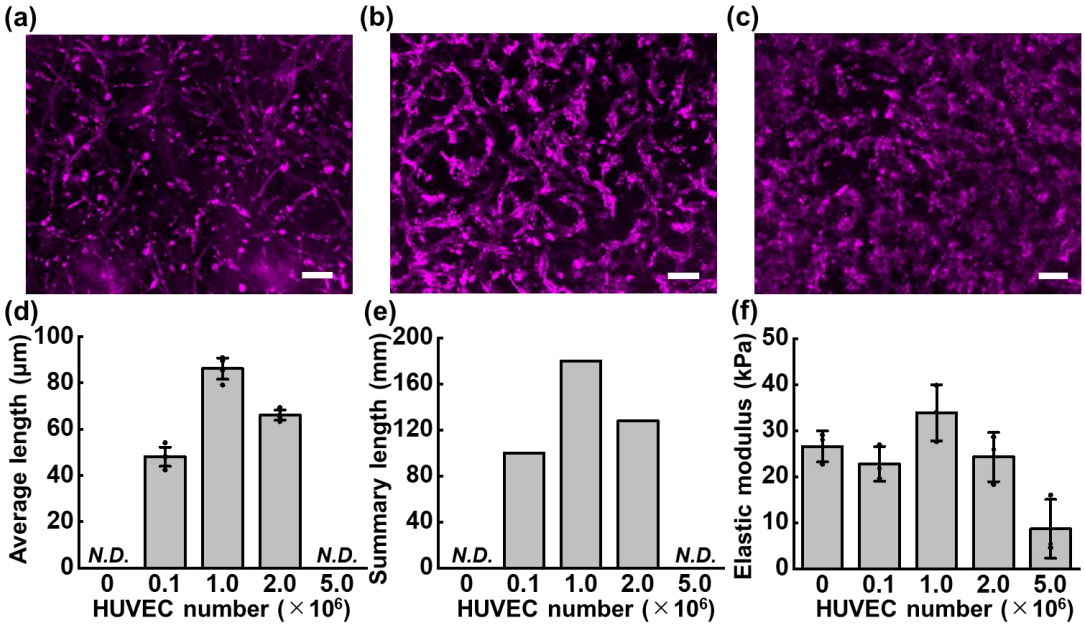

Figure 1-7. (a-c) Observation of blood capillary by CD31 immunostaining under CLSM. All of the samples have the same NHDFs number (1×10^6), the HUVECs number are 1×10^5 (a), 5×10^5 (b), 2×10^6 (c), scale bar = 100 μm, (d-e) The total and average length in a fixed area of 3D capillary structure calculated by ImageJ (*n*=5). (f) The stiffness of different 3D capillary tissue, the HUVECs number are 0 from 5×10^6.

experimental results, the average capillary length and stiffness of tissues increased first and then decreased with the increase of NHDF number. NHDF-1×10^6 showed the longest mean capillary length, reaching to 86 μm. However, when keeping the same number of NHDF and HUVEC increased from 5×10^5 to 1×10^6, the average length of capillaries increased significantly, which may mean that increasing the number of HUVEC is beneficial to the construction of 3D capillary networks.

Based on the above results, a new experimental condition was designed. The CMF amount was maintained at 3 mg, but the number of NHDF was fixed at 1×10^6, while the number of HUVEC was changed: 0, 1×10^5, 1×10^6, 2×10^6, 5×10^6. The experimental steps were as previously described: fluorescence images of stained tissues were obtained, the average length and total length of capillaries were calculated, and compression tests were also conducted, as shown in **Figure 1-7**. From the results, neither the average length nor the total length of capillaries increased with the increase in the number of HUVEC, which was similar to the results of the previous two experiments. This shows that tissue capillary growth is regulated by the number of both types of cells, and longer capillary length requires a balance between the

two cell types. In the above three experiments, the condition of 3 mg CMF, 1×10^6 NHDF, and 1×10^6 HUVEC contributed to the longest capillary length and suitable mechanical strength.

1.4 Conclusion

In this chapter, we reported on the generation of 3D capillary tissue and how the adjustment of CMF amount, NHDF number and HUVEC number affect the blood capillary growth. In the case of a fixed cell number, since NHDF can secrete collagen as a cross-linking agent to enhance tissue strength, increasing the amount of CMF reduced the number of cells per unit volume of the tissue and decreased the mechanical strength of the 3D tissue. When the amount of CMF was fixed, for NHDF or HUVEC, too few or too many cells per unit volume were not conducive to the growth of capillaries in 3D tissues, and NHDF and HUVEC synergistically regulated the growth of capillaries. We believe that the findings of this study have implications for tissue engineering techniques used to construct 3D capillary tissue *in vitro*.

1.5 Reference

[1] C. M. Niessen, D. Leckband, A. S. Yap, *Physiological Reviews* **2011**, *91*, 691.
[2] F. Louis, S. Kitano, J. F. Mano, M. Matsusaki, *Acta Biomaterialia* **2019**, *84*, 194.
[3] D. Su, C. L. Teoh, S.-J. Park, J.-J. Kim, A. Samanta, R. Bi, U. S. Dinish, M. Olivo, M. Piantino, F. Louis, M. Matsusaki, S. S. Kim, M. A. Bae, Y.-T. Chang, *Chem* **2018**, *4*, 1128.
[4] J. Li, N. Sasaki, K. Itaka, M. Terpstra, R. Levato, M. Matsusaki, *ACS Biomater. Sci. Eng.* **2020**, *6*, 5711.
[5] H. Liu, S. Kitano, S. Irie, R. Levato, M. Matsusaki, *Adv. Biosys.* **2020**, *4*, 2000038.
[6] Y. Naka, S. Kitano, S. Irie, M. Matsusaki, *Materials Today Bio* **2020**, *6*, 100054.
[7] W. T. Brinkman, K. Nagapudi, B. S. Thomas, E. L. Chaikof, *Biomacromolecules* **2003**, *4*, 890.
[8] X. Liu, W. Dan, H. Ju, N. Dan, J. Gong, *RSC Adv.* **2015**, *5*, 52079.
[9] D. M. Rogers, S. B. Jasim, N. T. Dyer, F. Auvray, M. Réfrégiers, J. D. Hirst, *Chem* **2019**, *5*, 2751.

Chapter 2

Control of capillary networks and hole structures by regulating elastic modulus of scaffolds in 3D Blood-Brain Barrier models

1.1 Introduction

The blood-brain barrier (BBB) is a type of capillary network characterized by a highly selective barrier, which restricts the transport of substances between the blood and nervous system.[1] Numerous *in vitro* models of the BBB have been developed for drug testing, but a BBB model with controllable capillary structures remains a major challenge.[2,3]

We have previously reported a 3D self-organized *in vitro* drop model of the BBB microvasculature which was produced by combining collagen microfibers (CMF) and fibrin gel.[4,5] The interconnected fibers play a crucial role in supporting the migration of brain microvascular endothelial cells (BMECs) and promoting the formation of capillary-like networks similar to those observed *in vivo*. Furthermore, a modified *in vitro* BBB model based on fibrin gel in a transwell insert was constructed, which also formed a 3D self-assembled microvascular network.[6] The presence of capillary opening holes on the bottom of the scaffold enabled the development of a perfusable microvascular system. This model showed higher high transendothelial electrical resistance (TEER) values relative to the acellular fibrin gels and 2D BMEC monolayers, demonstrating the BBB functional properties of this BBB model. In addition, the BBB model with more hole structure showed a higher transport ability of transferrin receptor (TfR) targeting antibody (AF 647-MEM-189), it is also revealed a higher TfR permeability of anti-TfR antibody (AF 647-MEM-189) than that of control isotype antibody (IgG1), thus demonstrating its potential for use in drug assessment. However, the mechanism of hole structure formation in this model has not been entirely clarified, and we have not identified if the capillary network structure could be regulated by changing the scaffold's mechanical properties.

In this chapter, we controlled the hole structure of a 3D *in vitro* BBB model by adjusting

the elastic modulus of the scaffold to reveal the mechanism of hole formation. The scaffold was constructed by the fibrin gel, which is an important part of the provisional ECM during wound healing. It can be used to observe the mechanical evolution of the ECM during the generation of capillary networks and hole structures because it has a wide range of adjustable mechanical moduli.[7–9] It was found that elastic modulus changes in the scaffold had a notable effect on the behavior of the BMECs, either inside or on the surface of the model. Shallower hole structures and dense internal capillary networks were obtained in the lower-stiffness scaffolds, whereas deeper hole structures were clearly observed in the stiffer scaffolds. In addition, RNA sequencing revealed that genes involved in ECM degradation, tight junction formation, angiogenesis, cell adhesion and migration were up-regulated in stiffer scaffolds. The results suggest the possibility of establishing precisely controlled hole and network structure for BBB models.

2.2 Experiments

2.2.1 Cell culture

The three cell lines used in this work have been developed and characterized in previous studies: human brain microvascular endothelial cells/conditionally immortalized clone 18 (BMEC),[10] human astrocytes/conditionally immortalized clone 35 (AC),[11] and human brain pericytes/conditionally immortalized clone 37 (PC) [12] were kindly provided by Prof. Furihata from the School of Pharmacy, Tokyo University of Pharmacy and Life Sciences (Hachioji, Tokyo, Japan). Cells were cultured on 225 cm2 collagen type I coated flasks (Ref. 4160-010, Iwaki, Shizuoka, Japan) or 100 mm diameter collagen type I coated dishes (Ref. 4020-010, Iwaki, Shizuoka, Japan) and incubated at 33 °C, 5 % CO_2. All culture media were supplemented with 4 μg/mL Blasticidin S HCl (Ref. R21001, Invitrogen, Waltham, USA) to maintain selective pressure during routine culture. BMECs were cultured in Vasculife (Ref. LEC-LL0005, VEGF-Mv, LifeLine, Frederick, USA) supplemented with 0.5 mL rh FGF-b, 0.5 mL ascorbic acid, 0.5 mL hydrocortisone hemisuccinate, 25 mL l-glutamine, 0.5 mL rh IGF-1, 0.5

mL rh EGF, 0.5 mL rh VEGF, 0.5 mL heparin sulfate, 25 mL fetal bovine serum (FBS) (kit, LifeFactor VEGF-Mv, LifeLine, Frederick, USA), 25 mL supplementary FBS (Gibco ThermoFisher, Waltham, USA), and 1% antibiotic (02892-54, Nacalai Tesque, Kyoto, Japan). AC were cultured in Dulbecco's Modified Eagle Medium (DMEM, Ref. 08458-16, Nacalai Tesque, Kyoto, Japan), complemented with 10% FBS, 1% antibiotic, 5 mL of N_2 supplement x100 (Ref. 17502-048, Gibco ThermoFisher, Waltham, USA). PCs were cultured in Pericyte Medium (Ref. 1201, ScienCell Research Laboratories, Carlsbad, USA), supplemented by 1 % Pericyte Growth Supplement 100x, 10 % FBS, and 1 % antibiotic. ACs and PCs were pre-differentiated at 37 °C for 3 days prior to use for the fabrication of the 3D BBB model.

2.2.2 Synthesis of FITC-labeled fibrinogen

The synthesis of fluorescein 5-isothiocyanate (isomer I) (FITC)-labeled fibrinogen was prepared as previously reported, with slight modifications.[13] First, 300 mg of fibrinogen (Ref. F8630-5G, Sigma Aldrich, St. Louis, MO, USA) was dissolved in 30 mL 0.1 M bicarbonate buffer (pH = 9, 0.1 M Na_2CO_3 : 0.1 M $NaHCO_3$ = 1 : 9) in a flask under stirring at 400 rpm. 30mg fluorescein 5-isothiocyanate (isomer I) (FITC, Ref. 16151-66, Nacalai, ≥ 90.0% (HPLC), Kyoto, Japan) was dissolved in 1 mL dimethyl sulfoxide (DMSO, Ref. 043-07216, FUJIFILM Wako, Chemical Pure, Osaka, Japan) in an Eppendorf tube. This FITC solution was then added to the fibrinogen solution under stirring at 400 rpm at room temperature, then left to react in the dark for 1 h at room temperature. The crude product was then transferred into a dialysis film (Mw: 12000-15000) and dialyzed in bicarbonate buffer for 3 days during which the buffer was changed 3 times every day. The buffer was changed to MilliQ water on the final day. Finally, the samples were freeze-dried (Freeze Dryer FDU-2200, Eyela, Tokyo, Japan) for 3 days to obtain FITC-fibrinogen sponge and kept in the dark before use.

2.2.3 Fabrication of 3D BBB models

First, a 10 wt% gelatin solution was prepared using gelatin powder (Ref. G1890, Sigma

Aldrich, St. Louis, MO, USA) dissolved in PBS. The gelatin solution was placed in a 37 °C water bath to completely dissolve it. Then, 450 µL of 10 wt% gelatin solution was dispensed on a 24-well plate (Ref. 3820–024, Iwaki, Shizuoka, Japan). The 0.4 µm pore size 24-well culture inserts (Ref. 3470, Costar, NY, USA) were carefully placed on the gelatin solution to ensure that no bubbles were formed below the insert. The 24-well plate was then incubated at 4 °C for 20 min to allow the gelatin solution to gelate. After gelation, the inserts were removed from the gelatin mold and culture insert membranes were peeled off. The membrane-free inserts were put inside a plasma device (Ref. PM100, Yamato Scientific Co., Ltd., Tokyo, Japan) at 40 sccm, 100 W for 1 min plasma treatment to make them hydrophilic. The plasma treated inserts were placed back onto the gelatin mold in the 24-well plate. The BMECs, ACs and PCs were harvested with a Trypsin/EDTA solution composed of 0.25 wt% trypsin (Ref. 209–19182, FUJIFILM Wako, Osaka, Japan) with 0.02 wt% EDTA (Ref. E6758-500G, Sigma Aldrich, St. Louis, MO, USA) and centrifuged at 130 g, 3 min, 25 °C. After centrifugation, the obtained cell pellets were resuspended in the medium and the cell count was measured using a Countess™ 3 Automated Cell Counter (Thermo Fisher, Waltham, USA). For the 3D BBB model, fibrinogen solutions were prepared using DMEM without FBS/antibiotics dissolved at concentrations of 10, 20, 30, 40, and 50 mg/mL (with 1 wt% pre-synthesized FITC-fibrinogen) and 40 µl of each solution was transferred to Eppendorf tubes. Then, 4×10^5 AC, 2×10^5 BMEC, 1×10^5 PC, and 0.2 U thrombin (Ref. T4648-10kU, Sigma Aldrich, St. Louis, MO, USA) were mixed in 20 µL of DMEM without FBS/antibiotics in another Eppendorf tube. The other BBB models in different conditions were prepared using a similar method, but with three variations of cell number inside the fibrin gel according to demand. Both solutions in the Eppendorf tube were mixed quickly before crosslinking, then the inserts were incubated at room temperature for 20 min to allow the fibrin gel to gelate. The final concentrations of fibrinogen were 7, 13, 20, 27 and 33 mg/mL. The samples were then incubated at 37 °C, 5% CO_2 for 40 min to make the gelatin mold revert to a liquid. After the gelatin melted, 500 µL of warmed PBS was added to the gap between the 24-well plates and the insert to wash away the liquid gelatin remaining on the outer wall of the inserts. The fibrin gels were placed in new 24-well plates with 2.5 mL of triple media comprising Vasculife medium, Pericyte medium, and DMEM/N_2 medium

(1:1:1; v:v:v), then incubated at 37 °C, 5% CO_2 overnight. On the next day, the pre-samples were inverted in a 6-well plate (Ref. 3810–006, Iwaki, Shizuoka, Japan) filled with 10 mL of triple media. More BMECs were harvested and 2×10^5 BMEC was resuspended in 60 μL of triple media, then seeded on the top surface of the fibrin gel samples for a second time. The samples were incubated at 37 °C, 5 % CO_2 for 6 h to ensure the adhesion of BMECs onto the fibrin gel. After incubation, the inserts were placed on top of 6-well culture plates with a specially designed 24- to 6-well plate adapter. An additional 2 mL of triple media was then added to make a total of 12 mL, and this was then incubated at 37 °C, 5% CO_2. Half of the media was changed (6 mL of the total 12 mL) every 3-4 days during the 7 days or 14 days of incubation.

2.2.4 Immunofluorescence staining

After 7 days or 14 days of incubation, the 3D BBB models were washed by warmed PBS 3 times then fixed in 4% paraformaldehyde (PFA, Ref. 30525-89-4, FUJIFILM Wako, Osaka, Japan) at room temperature for 1 h. Permeabilization was performed using 0.2% Triton X-100 (Sigma Aldrich, St. Louis, MO, USA) in PBS for 15 min at room temperature. The samples were washed again, then 1% bovine serum albumin (BSA, Ref. A3294-50G, Sigma-Aldrich, St. Louis, MO, USA) in PBS was used for blocking at room temperature for 25 min. The samples were then incubated with primary antibodies: monoclonal mouse anti-human CD31 antibody (Ref. M0823, DAKO, Denmark) diluted at 1/50 in PBS with 0.1% BSA overnight at 4 °C. After washing with PBS 3 times, the secondary antibody: goat anti-mouse secondary antibody (Alexa Fluor 647, Ref. A21235, Thermo Fisher Scientific, Waltham, MA, USA), nuclei stain Hoechst33342 (Ref. H3570, Thermo Fisher Scientific, Waltham, MA, USA), 1/100 dilution in PBS with 0.1% BSA were incubated for 2 h at room temperature in the dark. After washing with PBS 3 times, the samples were observed by confocal laser scanning microscopy (CLSM) (FluoView FV3000, Olympus, Tokyo, Japan) using 30 times magnification.

2.2.5 Mechanical elastic modulus measurements

All samples were removed from the medium after 7 or 14 days of culture and prepared for compression testing. Compression experiments were conducted to explore the mechanical behaviors under a 1 N loading cell by a 5 mm spherical indenter using an EZ-TEST instrument (Shimadzu, Kyoto, Japan) at a 1 mm/min loading speed. To eliminate any interference during the indentation, only the stable range of 5-10% stress in the stress-strain curve was considered and further fitted into a linear slope. Young's modulus of elasticity was automatically calculated by the instrument's own software.

2.2.6 Observation with optical coherence tomography (OCT)

An OCT system Cell3iMager Estier (SCREEN Holdings Co., Ltd., Kyoto, Japan) was used to confirm the hole structure of the *in vitro* 3D BBB model. After fixing the *in vivo* 3D BBB model, imaging was performed using OCT with an exposure time of 300 μsec, a scan size of 6000 μm × 6000 μm, a pitch of 7 μm, and a layer pitch of 50 μm. OCT images were processed using ImageJ software. Specifically, the hole structure in each slice of the OCT image was manually selected, then each slice image was masked with the selected hole structure. The masked multiple slices were finally merged to obtain a 3D image of the hole structure in BBB mode. The procedures were performed in the following order: freehand selections, Add to ROI manager, Mask, 3D viewer. The process with 14 slices and 34 slices of the masked images for the BBB models at 7 and 33 mg/mL fibrinogen concentration, respectively.

2.2.7 Calculation of blood capillary length

Blood capillaries from the fluorescence images were extracted and skeletonized by ImageJ software (Fiji, Ver. 1.53), [14] then their average length was analyzed and calculated by ImageJ. The procedures were performed in the following order: Gaussian Blur, Skeletonize (2D/3D), Analyze Skeleton (2D/3D).

2.2.8 RNA extraction from models

RNA extraction was performed on three types of 3D BBB models (n=2): ACs and PCs inside the fibrin gel with BMECs seeded on the bottom surface at 33 mg/mL fibrinogen ("Hol" group); ACs, PCs, BMECs inside the fibrin gel without BMECs on the bottom surface at 7 mg/mL fibrinogen ("Net" group); No cells inside the fibrin gel and BMECs seeded on the bottom surface at 33 mg/mL fibrinogen as a control group ("BM" group). Samples were first washed once in PBS and then transferred to 600 µL of Lysis Buffer (PureLink® RNA Mini Kit, Ref. 12183020, Thermo Fisher Scientific MA, USA) prepared with 1% of 2-mercaptoethanol, then the tissue was pipetted until fully dissolved. The homogenate was transferred to a sterile Eppendorf tube and centrifuged at 12,000 g for 2 min, then the supernatant was used for RNA extraction, following the PureLink® RNA Mini Kit protocol (Thermo Fisher Scientific, MA, USA). Extracted RNA was quantified using a NanodropTM N1000 device (Thermo Fisher Scientific, MA, USA).

2.2.9 RNA sequencing and data analysis

The above samples after RNA extraction were sent to the Genome Information Research Center (Osaka University, Japan) for RNA sequencing. Full-length cDNA was generated using a SMART-Seq HT Kit (Clontech, TaKaRa, Shiga, Japan) according to the manufacturer's instructions. An Illumina library was prepared using a NexteraXT DNA Library Preparation Kit (Illumina, California, USA) according to SMARTer kit instructions. Sequencing was performed on an Illumina NovaSeq 6000 sequencer (Illumina, California, USA) in the 100-base single read mode. Sequenced reads were mapped to the human reference genome sequences (hg19) using TopHat version 2.1.1. The fragments per kilobase of exons per million mapped fragments (FPKM) were calculated using Cuffnorm version 2.2.1. The raw data have been deposited in the NCBI's Gene Expression Omnibus database. The iDEP (http://bioinformatics.sdstate.edu/idep/) differential expression analyses and global analysis of the RNA-sequencing expression data were performed using BioJupies

(https://amp.pharm.mssm.edu/biojupies/).[15] Gene Ontology and Pathway Enrichment (WikiPathways_2021 library) and analysis results were generated by analyzing the up-regulated and down-regulated gene sets using Enrichr. The up-regulated and down-regulated gene sets were generated by extracting the 500 genes with the respectively highest and lowest values of T-score from the gene expression signature, then submitted to Enrichr and plotted.[16,17]

2.2.10 Statistical analysis

All data are expressed as means ± SD. The values represent the means ± SD from three independent experiments, unless otherwise stated. Statistical comparisons between groups were analyzed using two-tailed Student's t-tests. A value < 0.05 was considered statistically significant. These are indicated in the graphs as $*p < 0.05$, $**p < 0.01$. N.D. denotes not detected. N.S. denotes no significant difference.

2.3 Results

2.3.1 Influence of the fibrin gel stiffness on the BMEC capillary network and hole formation

First, we fabricated a 3D BBB model using BMECs, ACs and PCs seeded in inside the fibrin gel and BMECs seeded on the bottom surface of the fibrin gel with varying stiffnesses to investigate the BMECs behavior in this model. Different stiffnesses could indeed be achieved by varying the fibrinogen concentration,[18] from 7 mg/mL (soft) to 33 mg/mL (hard). As shown in **Figure 2-1a**, structural changes were observed in the holes and a capillary network was formed by BMECs in the fibrin gels with different stiffnesses. After immunostaining, all 3D BBB models were observed with confocal laser scanning microscopy (CLSM) at different depths in the fibrin gel. In this 3D BBB model, BMECs on the bottom surface can form a

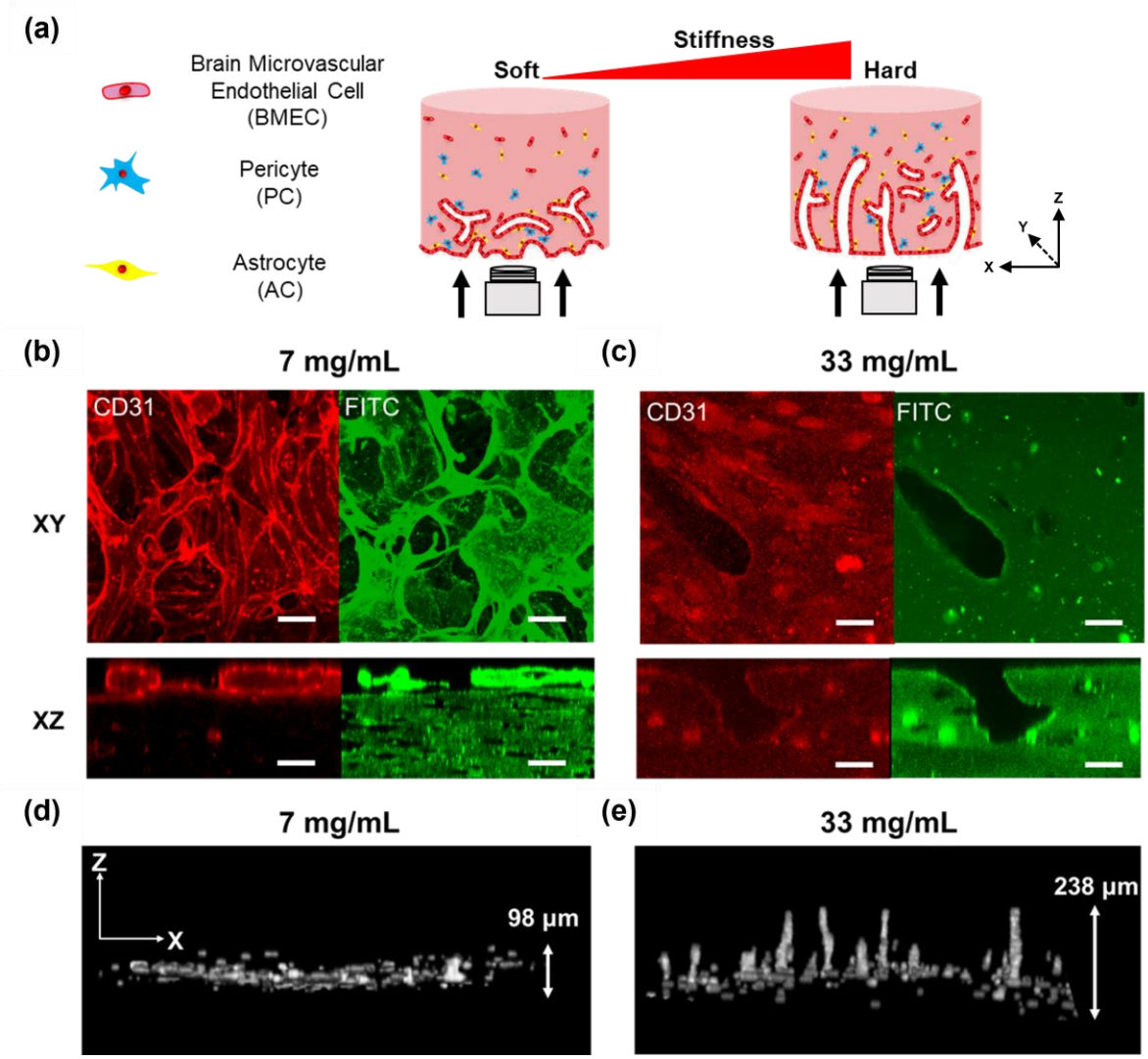

Figure 2-1. (a) Schematic illustration of network and hole formation depending on the stiffness of scaffolds, and CLSM observation position in the 3D BBB models. (b-c) CLSM images of CD31 immunostaining and FITC-fibrin gel in 3D BBB models at different fibrinogen concentrations of 7 and 33 mg/mL, after 14 days of incubation. Scale bar: 30 μm. (d-e) 3D reconstruction images of the hole structures in the 3D BBB models obtained by OCT at 7 (left) and 33 (right) mg/mL fibrinogen concentration, after 14 days of incubation. The Z axis was enlarged 5 times by ImageJ.

monolayer and migrate over time to form hole structures, while the BMECs seeded inside the fibrin gel can form a capillary network. We also performed compression testing on all samples to verify and analyze the effect of fibrinogen concentration on the model elastic modulus. For this construction, we first discovered that 3D BBB models with hole structures of different depths could be generated by controlling the elastic modulus.

Figure 2-1(b-c) show fluorescence images obtained by CLSM. The samples were immunostained for CD31 in the FITC-labeled fibrin gel. CD31 is a typical marker of

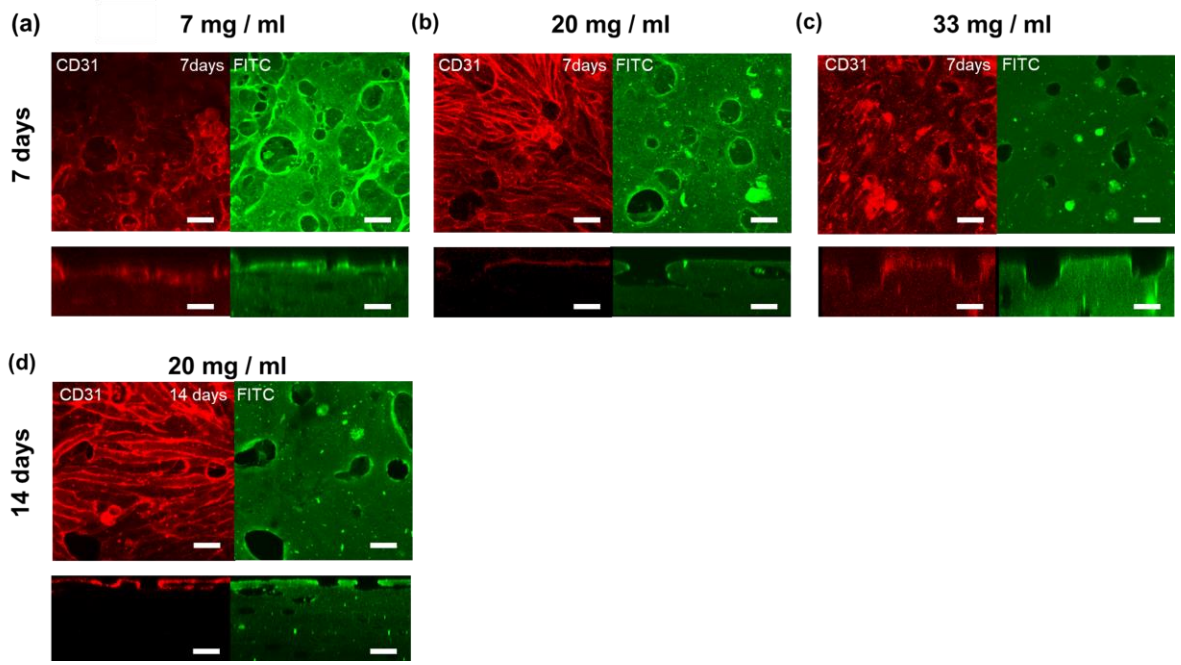

Figure 2-2. CLSM images of CD31 immunostaining and FITC-fibrin gel in the surface position (XY plane, 0~30 μm) and Z direction of BBB models at different fibrinogen concentrations of **(a-c)** 7~33 mg/mL, after 7 days of incubation, and **(d)** 20 mg/mL, after 14 days of incubation. Scale bars are 30 μm.

endothelial cells commonly used for observing the capillary network structure formation. The FITC-fibrinogen's photochemical stability allows it to maintain a high intensity over long periods of fluorescence exposure, which was preferable for hole structure observation and analysis. **Figure 2-1(b-c)** and **Figure 2-2** show samples after 14 days of incubation, where we found some sub-circular structures on the surface with extensions to the interior of the gel, named hole structures. The CD31-stained and FITC images clearly show the hole structure (XY planes) and side view (XZ planes) of the models. At a low concentration of fibrinogen, it can be seen that many holes were formed and their extension to the interior (Z-direction) is shallow. At higher fibrinogen concentrations (especially at 33 mg/mL), there were fewer holes formed on the surface of the model, but deep holes were formed that were internally connected to the outside environment. **Figure 2-1(d-e)** shows 3D BBB models observed by optical coherence tomography (OCT) and processed by ImageJ. The range of the images is after calculation and shows the Z-direction depth in the 3D BBB models with 7 and 33 mg/mL fibrinogen concentrations is 98 μm and 234 μm, respectively. It also demonstrates the difference of hole depth in the soft and hard 3D BBB models.

2.3.2 Influence of elastic modulus on the capillary network inside the 3D BBB models

To further characterize the relationship between fibrinogen concentration and elastic modulus in fibrin gels, the elastic modulus of acellular fibrin gels and 3D BBB models at different fibrinogen concentrations (7, 13, 20, 27, and 33 mg/mL) was measured by compression testing, as shown in **Figure 2-3a**. In both the acellular fibrin gel and BBB models groups, the elastic modulus increased with an increase in fibrinogen concentration, due to the

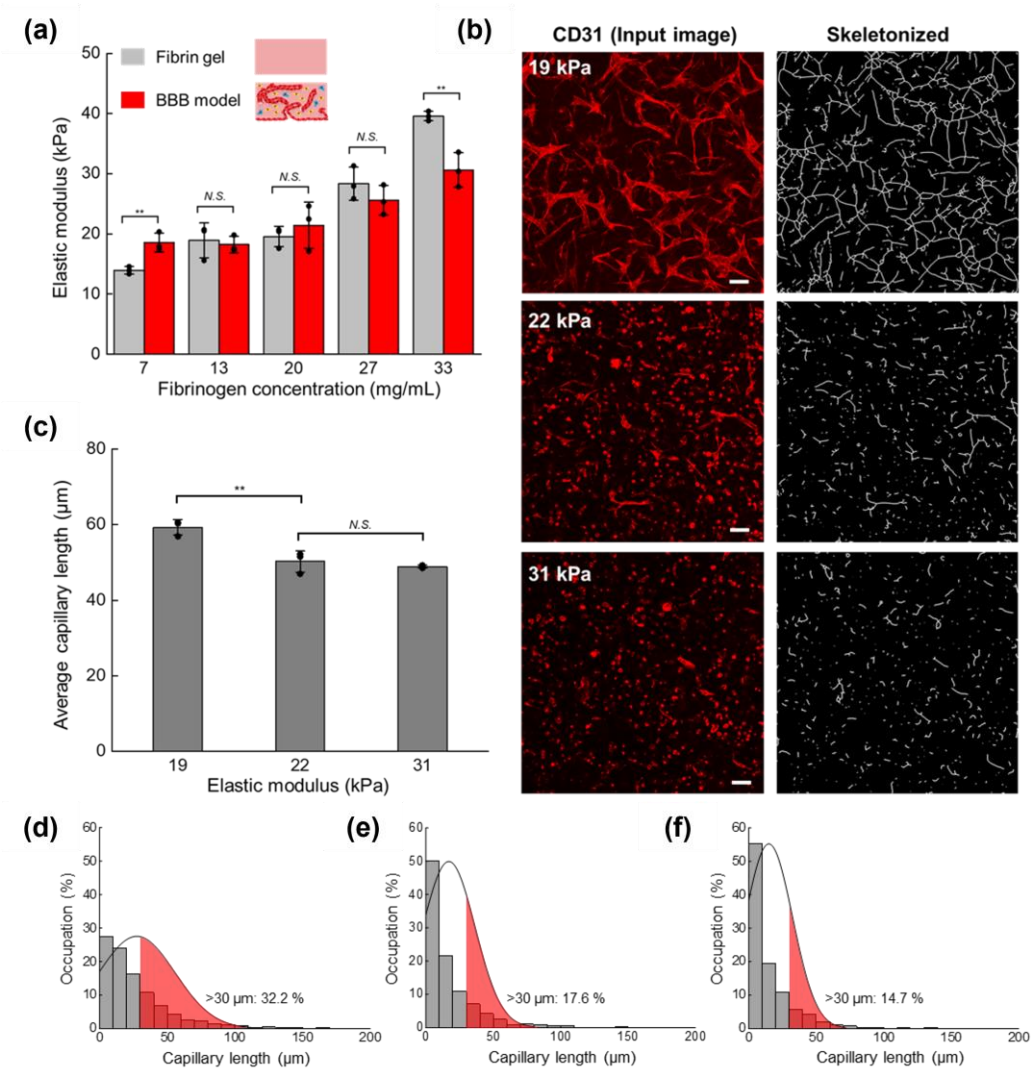

Figure 2-3. (a) Elastic modulus of 3D BBB models after 7 days of incubation by compression testing. (b) CLSM image for blood capillary network structure in the 3D BBB models at 19~31 kPa after CD31 immunostaining and the skeletonized images processed by ImageJ software. Scale bar: 100 μm. (c) Calculated blood capillary length of 3D BBB models at 19~31 kPa by ImageJ software (n=3). Data are presented as means ± S.D. (d-f) The ratio and normal distribution of capillary length of 3D BBB models at 19 (d), 22 (e), 31 (f) kPa.

raised crosslinking degree in the fibrin gel. In samples with 7 mg/mL fibrinogen concentration, the 3D BBB models had a higher elastic modulus than acellular fibrin gel, but at a high fibrinogen concentration of 33 mg/mL, the acellular fibrin gel had a higher elastic modulus than the 3D BBB models. We hypothesized that the formation of a capillary network influences the connection structure inside the models and has an impact on the elastic modulus changes so we evaluated the capillary network in the 3D BBB models. **Figure 2-3b** shows capillary network confocal fluorescence images at 7 days culture in the 3D BBB models with an elastic modulus of 19, 22 and 31 kPa (7, 20 and 33 mg/mL). At a low elastic modulus (19 kPa), the BMECs formed a connected capillary network. However, at a high elastic modulus (22 and 31 kPa), most of the BMECs existed as single cells, while only a few formed short capillaries. To quantify the capillary length, ImageJ software was used to extract the skeletal outline of the capillary network at each concentration. The average length of the extracted skeleton was calculated as shown in **Figure 2-3c**. From **Figure 2-3b**, we can quantify the size of a CD31 positive spot (BMEC aggregation) at around 15 μm, so statistics larger than 2 spots (30 μm) were counted. From the calculated data, the average capillary lengths of the models were 59.3 μm, 50.2 μm and 48.9 μm for the 3D BBB models with a respective elastic modulus of 19, 22, and 31 kPa (**Figure 2-3c**). These data cannot fully describe the relationship between concentration and capillary length, so the percentage of interval length of capillaries and a normal distribution plot were calculated. As shown in **Figure 2-3(d-f)**, 32.2% of the capillaries were longer than 30 μm in the models with an elastic modulus of 19 kPa, but only 14.7% in those of 31 kPa models. These results demonstrate that capillary formation becomes difficult inside 3D BBB models under conditions of increasing elastic modulus, which is consistent with previous works,[19–21] indicating that the internal structure of the model can be regulated by adjusting the scaffold stiffness.

2.3.3 Influence of elastic modulus and culture time on the hole structure formation

We next performed quantitative analysis of the hole structure to gain further insights into

the effect of differences in elastic modulus and culture time. Quantitative analysis of the hole structures' number, diameter, and depth was based on FITC fluorescence images, as CD31 staining is susceptible to attenuation from prolonged irradiation and produces weaker signals in deeper regions of the 3D BBB model, while FITC-fibrinogen has a stronger signal and responds to the physical morphology of the hole structure. Therefore, to demonstrate the overlap of CD31 and FITC signals, colocalization analysis of CD31 and FITC images was required. **Figure 2-4a** shows the method of colocalization analysis using Imaris software. A hole structure was first selected, FITC and CD31 in the same area were quantified separately using Imaris to obtain two specific values of fluorescence intensity, and then the percentage of colocalization was calculated by dividing the average fluorescence intensity value of CD31

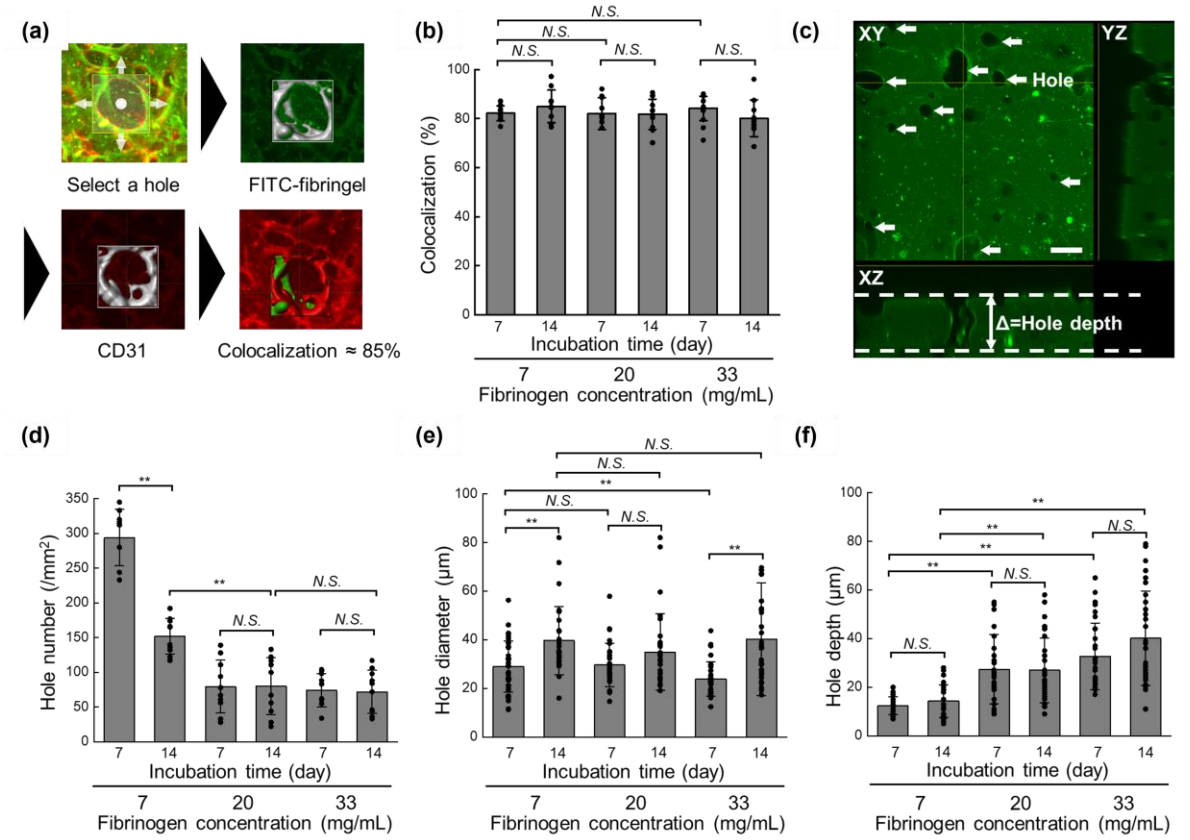

Figure 2-4. (a) Hole structure colocalization between CD31 and FITC-fibrin gel images, colocalization was calculated by Imaris. (b) The calculated colocalization at 7~33 mg/mL fibrinogen concentration after 7 and 14 days of incubation (n=10). N.S. means no significant differences. (c) Representative CLSM image of FITC-fibrin gel to describe hole position (arrow) and depth (double arrow). Scale bar: 50 μm. Calculated hole (d) number, (e) diameter, (f) depth of the 3D BBB models at 7~33 mg/mL fibrinogen concentration after 7 and 14 days of incubation (n=10 for number, n=30 for diameter and depth, respectively). Data are presented as means ± S.D.

with the average fluorescence intensity value of FITC. As shown in **Figure 2-4b**, 10 different holes were selected at different locations on each sample to ensure accuracy and reproducibility. The results showed a colocalization percentage of FITC and CD31 of more than 80% on all samples. The FITC fluorescence images can therefore be used for the characterization of the holes. **Figure 2-4c** show the location of the hole (white arrow), the XZ planes image shows the hole clearly and the hole depth can be calculated by measuring the difference between the lowest and highest positions (double arrow). From the calculation results, the number of holes was greatest in the low elastic modulus condition (290 holes/mm^2). Although there were fewer holes for models after 14 days of culture (150 holes/mm^2), they were still about two times higher than the numbers for the 20 mg/mL and 33 mg/mL fibrinogen models. For the 20 mg/mL and 33 mg/mL fibrinogen models, there were no significant changes in the number of holes for models after 7 or 14 days of culture (**Figure 2-4d**). The size of the hole was also calculated (**Figure 2-4e**). It was found that the hole diameter of most models was not significantly different in the same culture time, around 25~40 μm, and only the 33 mg/mL model after 7 days culture was found to have smaller holes than the 7 and 20 mg/mL models. For models with the same fibrinogen concentration, the diameter of the holes showed a trend of increasing with increasing culture time. For the models at 7 mg/mL fibrinogen concentration, in relation to the results of hole number, it was demonstrated that a longer culture time led to an increase in hole size and finally the number of holes decreased. With the increase of fibrinogen concentration, the average depth of the holes increased, reaching around 80 μm in the 33 mg/mL models (**Figure 2-4f**). At the same fibrinogen concentration, the average depth of the holes in all samples was not significantly changed by culture time. However, according to the figure, the average hole depth showed a trend of becoming slightly deeper with increasing culture time.

The quantitative analysis is in accordance with the qualitative observation obtained from the CLSM images in **Figure 2-1**. It shows various properties of holes in the 3D BBB models, such as size and number, can be adjusted by varying the scaffold elastic modulus, which has important implications for the fabrication of a controllable 3D BBB model.

2.3.4 Effect of elastic modulus and BMEC seeding density on the hole formation

For the 3D BBB model in this study, the proliferation and migration of BMECs on the bottom surface contribute to the hole formation, but the exact mechanism of this formation remains unclear. Therefore, we investigated if the BMEC seeding density on the bottom surface of the hydrogel would impact the hole formation. The seeding densities of BMECs on the bottom surface in 3D BBB models were thus changed to 2×10^3, 4×10^3, and 2×10^4, which was

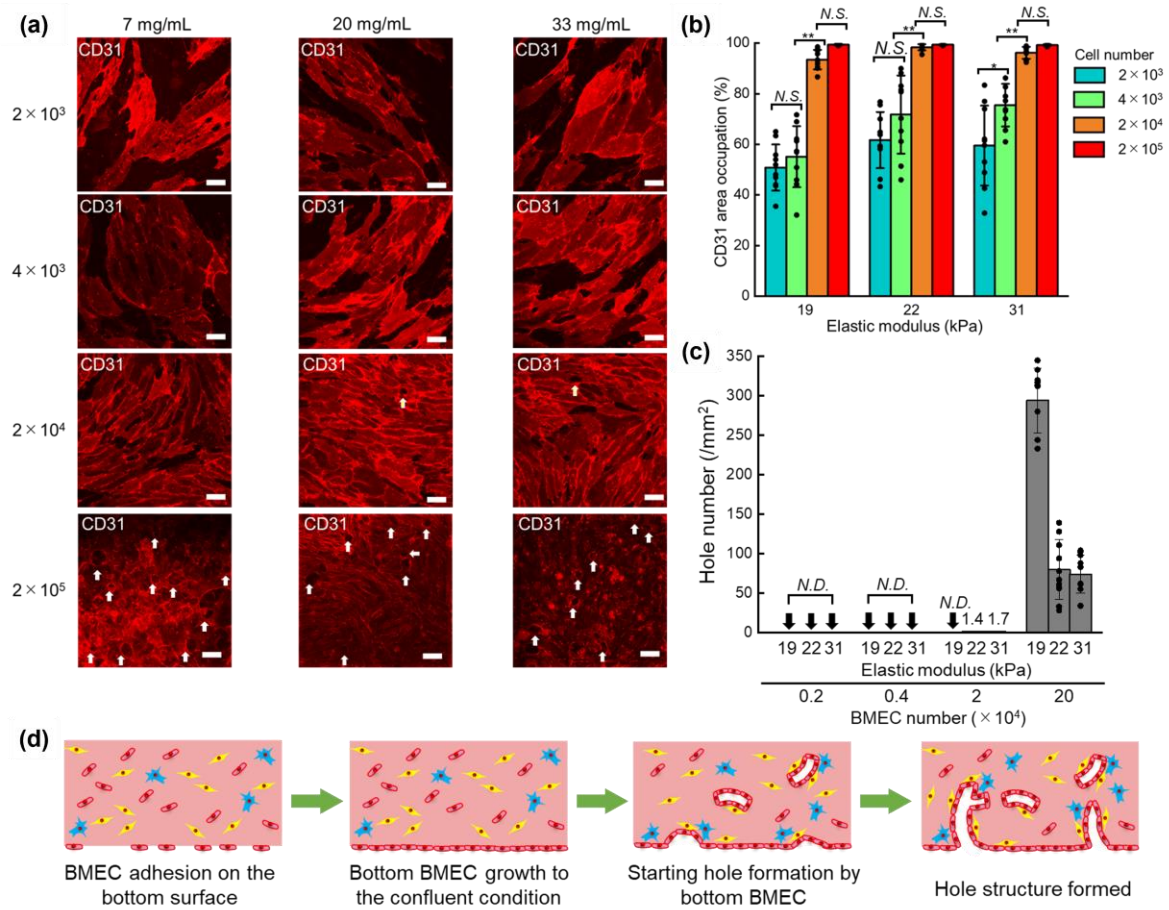

Figure 2-5. (a) CD31 immunostaining images of the 3D BBB models at 7~33 mg/mL fibrinogen concentration by varying seeding BMEC density to the bottom surfaces after 7 days of incubation. Scale bar: 50 μm. (b) CD31 area occupation of 3D BBB models with 19~31 kPa elastic modulus with different BMEC seeding density at 0.2, 0.4, 2 and 20×10^4, respectively (n=10). (c) Calculated hole numbers of 3D BBB models with 19~31 kPa elastic modulus by varying BMEC seeding density at 0.2, 0.4, 2 and 20×10^4, respectively (n=10). Data are presented as means ± S.D. (d) Schematic illustration of growth and hole structure formation processes of the bottom BMECs.

100, 50, and 10 times lower than the 2×10^5 BMECs on the original 3D BBB models' surface. After 7 days of incubation, models were immunostained by CD31 and the fluorescence images were also obtained by CLSM as shown in **Figure 2-5a**. The elastic modulus values for the 3D BBB models with different fibrinogen concentrations were 19 (7 mg/mL), 22 (20 mg/mL), and 31 kPa (33 mg/mL) obtained from **Figure 2-3a**. Independently of elastic modulus, were not formed in the models with $0.2x10^4$ and $0.4x10^4$ BMECs, due to the insufficient BMECs coverage on the bottom surface. Even for the 2×10^4 models, only a few holes were found in the high concentration condition. Quantitative analysis of CD31 area occupation was calculated by ImageJ software and the hole number was counted (**Figure 2-5(b-c)**). Even in 3D BBB models with different elastic moduli, as the BMEC seeding density increased, the coverage of BMECs gradually increased from 50% to around 70% in the models with 0.2×10^4 and 0.4×10^4 up to around 95% in the 2×10^4 model, but the hole structures density was only 1.4 and 1.7/mm2, which was much lower than the original 3D BBB model. This shows that BMECs did not migrate to the inside of the model at a lower BMEC seeding density.

From these results, we described the potential mechanism of BMEC behavior during the formation process of hole structures at a low BMEC seeding density condition as shown in **Figure 2-5d**. After BMECs are seeded and adhere to the bottom surface of the 3D BBB model, they gradually grow to form a confluent monolayer. After the BMECs on the surface reach a certain number, they may start to migrate inside the fibrin gel, and eventually these migration behaviors may make the hole appear on the surface of the 3D BBB models.

2.3.5 Time lapse of hole formation in the 3D BBB model

To investigate the changes in the 3D BBB model during culture which lead to the formation of the hole structure, the elastic modulus and CD31 immunostaining was performed on the 3D BBB model was evaluated after 1 and 3 days of incubation. **Figure 2-6a** shows the time-dependent changes of elastic modulus of the acellular fibrin gel and 3D BBB model with a fibrinogen concentration of 7 and 33 mg/mL. In the acellular fibrin gel group, we found almost no change in the elastic modulus after different culture times irrespective of fibrinogen

concentration. On the other hand, in the 3D BBB model groups, the elastic modulus of the 33 mg/mL fibrinogen models decreased with increasing culture time (37 kPa to 31 kPa), whereas 7 mg/mL fibrinogen models showed increased elastic modulus with increasing culture time (13 kPa to 19 kPa). **Figure 2-6b** shows CLSM images for acellular FITC-fibrin gel after 7 days of culture at 7 and 33 mg/mL fibrinogen concentration. The surface of the incubated fibrin gel was smooth, with no hole structure, which excluded the possibility that hole structure formation was due to the self-degradation of fibrin gel in a 3D BBB model. **Figure 2-6c** shows projection images of the 3D BBB model with a Z range of 20 μm for all conditions, starting from the bottom to the inside of the models. Overall, BMECs had aggregated on the surface of the 3D BBB models at day 1, while also starting to invade the interior of the gel. At day 3, the BMECs on the surface congregated, forming a monolayer, and a few hole structures also appeared, as also shown in Movie S1. Furthermore, for the 3D BBB models with different elastic moduli,

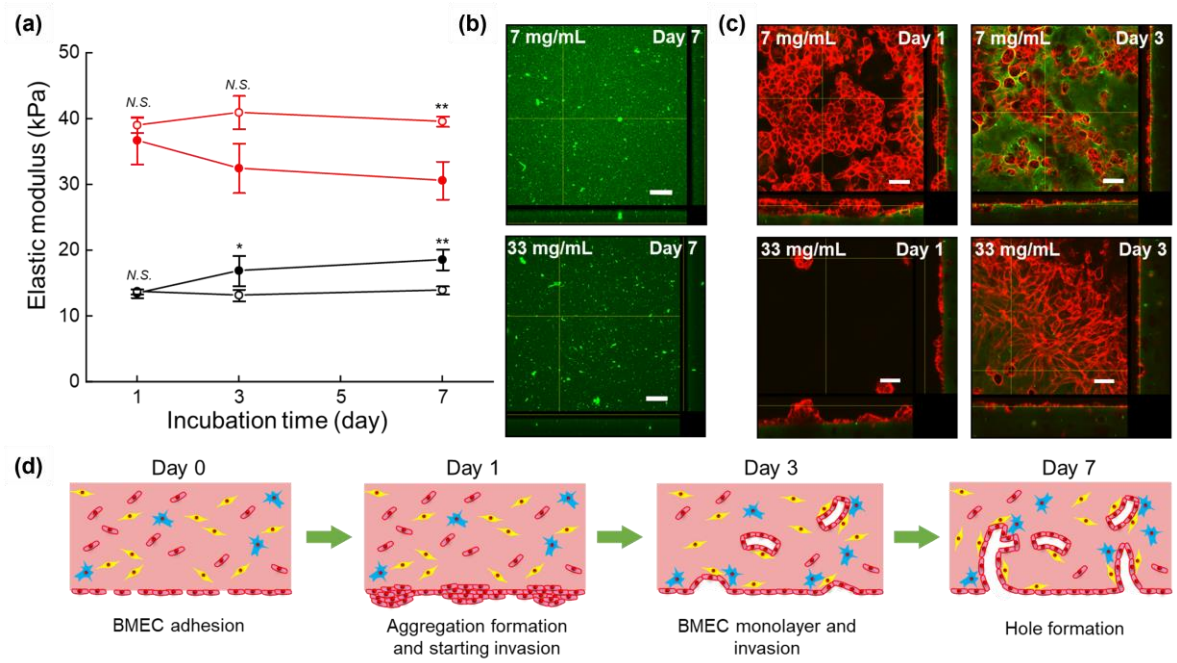

Figure 2-6. (a) Elastic modulus of 3D BBB models after 1~7 days incubation by compression testing. The fibrinogen concentration is 7 (black) and 33 mg/mL (red), the model is an acellular fibrin gel (○) and a 3D BBB model (●), respectively (n=3). Data are presented as means ± S.D. (b) CLSM images of acellular FITC-fibrin gel at 7~33 mg/mL fibrinogen concentration after 7 days of incubation. Scale bar: 50 μm (c) CLSM images of 3D BBB models at 7~33 mg/mL fibrinogen concentration after 1 or 3 days of incubation, the Z range is 20 μm for all conditions. Scale bar: 50 μm. (d) Schematic illustration of bottom BMEC behavior over the time leading to the hole formation.

we observed similar BMECs morphology on day 1. However, on day 3, more hole structures had started to form on the surface of softer (7 mg/mL) 3D BBB models, the BMECs had formed a confluent layer and a few hole structures had started to form on the surface of harder (33 mg/mL) 3D BBB models. This suggests that at the early period of hole structure formation, BMECs already generate expression differences on the surface of the 3D BBB model with different elastic moduli. From these results, the potential mechanism of the time-dependent structural changes leading to the formation of hole structure is summarized in **Figure 2-6d**. After the BMECs adhered to the bottom of the model, they proliferated, formed cell aggregates, and started to migrate inside the model. Subsequently, the BMEC monolayer and holes formed with continued incubation.

2.3.6 Incorporation of supporting cells on the hole structure formation of scaffolds with different stiffnesses

We next evaluated the effects of ACs and PCs on hole structure formation in the different elastic modulus 3D BBB models. Although the BBB model configuration differed from the original BBB model, it was estimated that the increased fibrinogen concentration would have a similar impact on the stiffness of the fibrin gel, as seen in **Figure 2-2a**. Varying the fibrinogen concentration from 7 to 33 mg/mL would thus lead to the formation of a soft and hard gel, respectively. As seen in **Figure 2-7(a-d)**, a modified model was prepared by removing cells inside the fibrin gel and with only BMECs seeded on the bottom surface, named the "BM" model. After 7 days of incubation, no hole structures were detected on any of the 3 types of BM models, independently of the fibrinogen concentrations used. The models of ACs and PCs (w/o BMECs) inside the fibrin gel with surface BMECs were also evaluated, as shown in **Figure 2-7(e-h)**. A hole structure was found at all concentrations of models, demonstrating that ACs and PCs have an important role in promoting the formation of a hole structure. This could be due to the secreted factors by ACs and PCs, such as vascular endothelial growth factor (VEGF), basic fibroblast growth factor (bFGF), and angiopoietin 1 (ANG-1).[22] The hole number of w/o BMEC models were 152 (7 mg/mL), 49 (20 mg/mL), and 42 holes/mm^2 (33

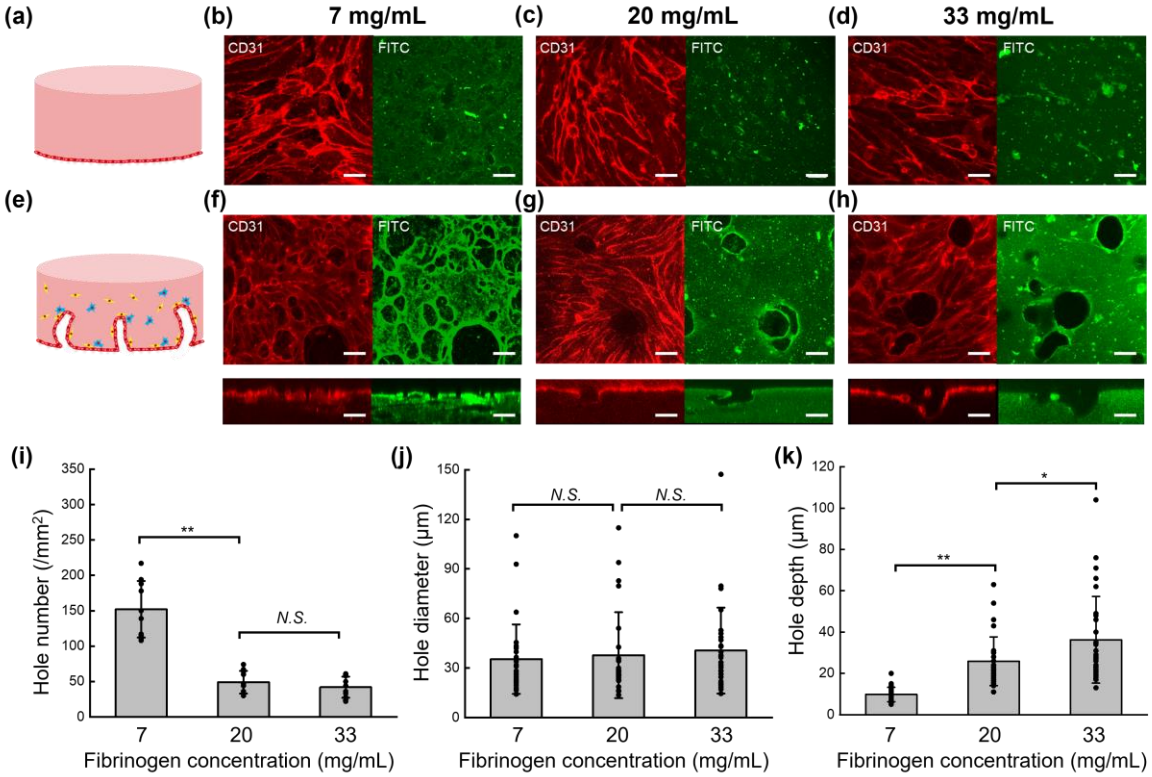

Figure 2-7. (a) Schematic illustration of the model without cells inside the fibrin gel and only BMECs on the bottom surface. (b-d) CLSM images of CD31 immunostaining and FITC-fibrin gel in samples without cells inside the fibrin gel with a bottom BMEC monolayer at different fibrinogen concentrations of 7~33 mg/mL, after 7 days of incubation. Scale bar: 30 μm. (e) Schematic illustration of the model without BMECs inside the fibrin gel. (f-h) CLSM images of CD31 immunostaining and FITC-fibrin gel in samples without AC and PC cells inside the fibrin gel with a bottom BMEC monolayer at different fibrinogen concentrations of 7~33 mg/mL, after 7 days of incubation. Scale bar: 30 μm. Calculated hole (i) number, (j) diameter, (k) depth of samples without AC and PC cells inside the fibrin gel and with a bottom BMEC monolayer at 7~33 mg/mL fibrinogen concentration after 7 days of incubation (n=10 for number, n=30 for diameter and depth, respectively). Data are presented as means ± S.D.

mg/mL), showing that the model with the low fibrinogen concentration yielded the highest value (**Figure 2-7i**). For calculated hole diameter, there were no significant differences between any of the models (**Figure 2-7j**). The calculated hole depths were 10, 26, and 36 μm for the 7, 20 and 33 mg/mL fibrinogen concentrations, respectively (**Figure 2-7k**). These values are within the same range as the original 3D BBB models. The phenomenon of more and shallower hole structures for the soft model (7 mg/mL) and fewer and deeper hole structures for the hard model (33 mg/mL), is in accordance with the observations from **Figure 2-3**.

2.3.7 Gene expression analysis

RNA sequencing was performed to investigate the effect of hole structure formation on gene expression. Three types of models were designed, the hole structure model (Hol), the capillary network model (Net) and only BMECs on the model bottom surface (BM), as shown in **Figure 2-8(a-c)**. All the models were incubated for 7 days, and then total RNA was collected and sequenced for comparison. To evaluate the functional effects of these gene expression changes, we performed GO enrichment analysis of the up and down-regulated genes. The up-regulated terms of Hol vs Net, Hol vs BM, and Net vs BM are shown as in **Figure 2-8(d-f)**. These terms are GO biological process, molecular function, and cellular component, respectively, and the results are sorted in order of decreasing p-value. From these differences, it seems that the enrichment terms related to protein cleavage, extracellular matrix, cytokines, and lysosomes are important in Hol. For BM, both Hol and Net show enrichment terms associated with proliferation (mitosis). The above results show that Hol and Net have extremely similar gene expression due to the same cell types, initial BMEC, AC, and PC seeding numbers and culture times used in these models. Therefore, in the analysis of key genes in cell adhesion, cell migration, focal adhesion, tight junction formation, angiogenesis, and ECM degradation, we considered genes with fold changes that had a relatively large value to be differentially expressed genes. The heat map of the selected key genes in each sample is shown in **Figure 2-8g**, showing differential properties of these genes in Hol, Net, and BM. Compared to Net, 12 genes were up-regulated in Hol and these genes may be associated with the formation of holes. Therefore, the specific fold changes of the differential genes were counted and are summarized in **Figure 2-8(h-i)**. From the results, MMP1, MMP10, ACE genes coding for ECM and protein degradation; CLDN5 coding for the tight junction protein Claudin-5; ITGA1, CD36 coding for proteins involved in cell adhesion; ANGPT1, ANGPTL1, COL21A1 coding for proteins involved in angiogenesis processes; FZD1 coding for focal adhesion, were up-regulated in Hol compared to Net.

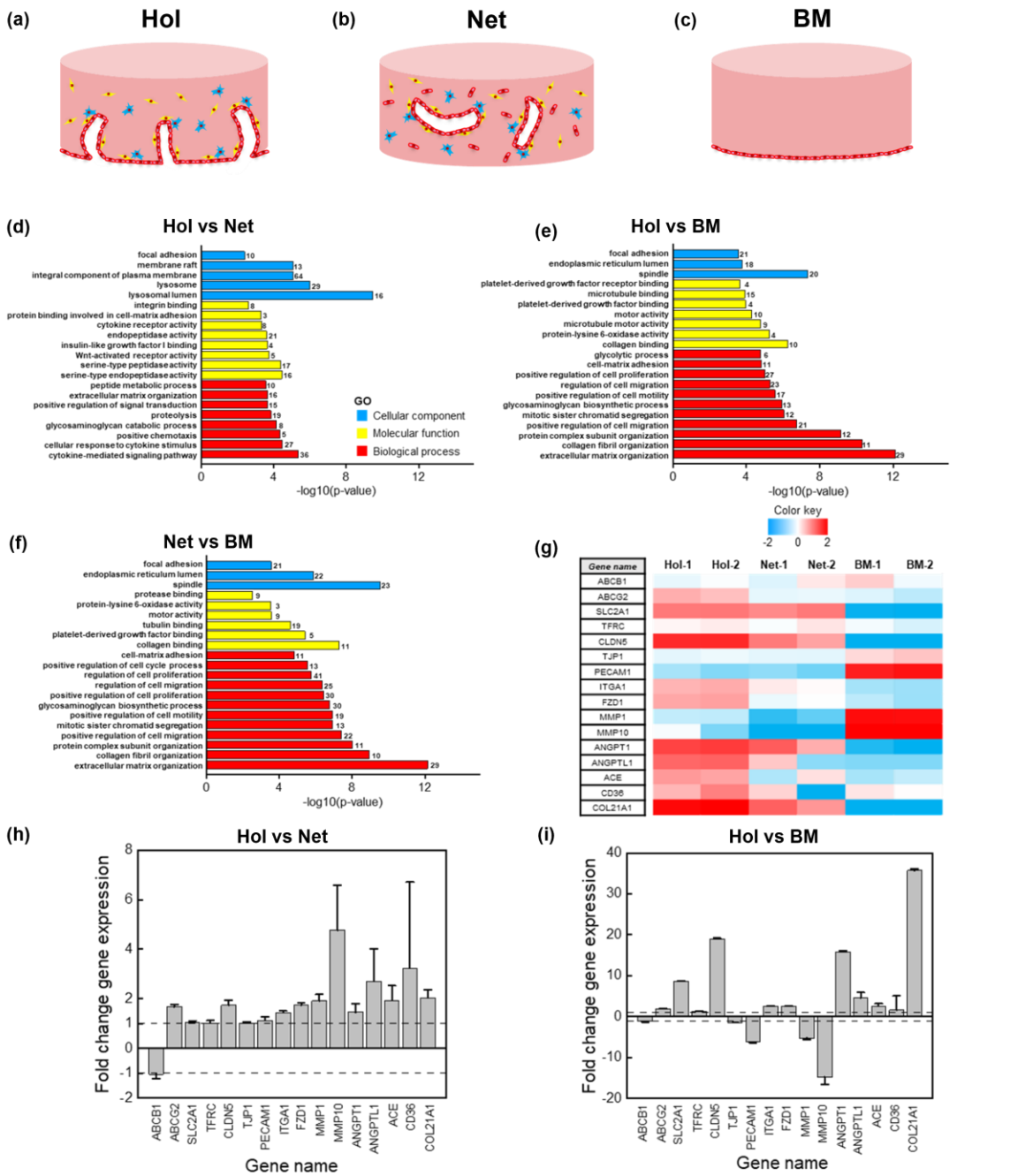

ABCB1 (ATP binding cassette subfamily B member 1): Permeability glycoprotein, transporter
ABCG2 (ATP binding cassette subfamily G member 2): BCRP, transporter
SLC2A1 (solute carrier family 2 member 1): GLUT1, transporter
TFRC (Transferrin receptor 1): TfR, transporter
CLDN5 (Claudin-5): Tight junction protein
TJP1 (Tight Junction Protein 1): ZO-1, tight junction
PECAM1 (Platelet And Endothelial Cell Adhesion Molecule 1): CD31, endothelial marker
ITGA1 (Integrin alpha-1): Collagen receptor, related to cell adhesion and migration
FZD1 (Frizzled class receptor 1): Focal adhesion, Wnt signaling protein receptor
MMP1 (Matrix Metallopeptidase 1): ECM degradation
MMP10 (Matrix Metallopeptidase 1): ECM degradation
ANGPT1 (Angiopoietin 1): Regulation of angiogenesis, endothelial cell survival, proliferation, migration, adhesion
ANGPTL1 (Angiopoietin Like 1): Vascular endothelial growth factor
ACE (Angiotensin I converting enzyme): CD143, Proteolysis
CD36 (Cluster of differentiation 36): cell adhesion molecule
COL21A1 (Collagen Type XXI Alpha 1 Chain) : Vascular formation, collagen

Figure 2-8. RNA sequencing comparison of 3 types of models (n=2); (a) ACs and PCs inside the fibrin gel with BMECs on the bottom surface at 33 mg/mL fibrinogen, a hole structure formed on the model surface but without a capillary network inside. (b) ACs, PCs, BMECs inside the fibrin gel without cells on the bottom surface at 7 mg/mL fibrinogen, a capillary network formed inside the model but without a hole structure on the model bottom surface. (c) Without cells inside the fibrin gel and only BMECs on the bottom surface at 33 mg/mL fibrinogen as a control group, neither hole nor capillary networks could be formed. (d-f) The gene ontology (GO) of biology process, molecular function, cellular component terms for up-regulated genes in Hol vs. Net (control) group, Hol vs. BM (control) group, Net vs. BM (control) group, respectively. The number on each term bar is the number of genes contained. (g) Heatmap shows the different gene expression pattern of BBB transporter, tight junction formation, cell adhesion, cell migration and angiogenesis. (h-i) The different expression of genes in Hol respectively compared to Net and BM, were represented by the calculation of gene fold change (n=2). Genes with fold change values greater than 1 are up-regulated, those with fold change values less than -1 are down-regulated. Data are presented as means ± S.D.

2.4 Discussion

Herein, based on a reported method in our laboratory, we attempted to build an *in vitro* model of a BBB, which has a hole structure on the model surface to effectively connect the model inside the microenvironment with the outside environment for transportation. The hole structure is similar to the lumen structure in the process of vascular sprouting. Specifically, new vascular sprouting is guided by endothelial tip cells and forms a lumen structure after proliferation and migration of endothelial stalk cells.[23] The formation of lumen structure is often found in the interior of models such as 3D microfluidic chips.[24] However, we found for the first time that the formation of lumen structure on the tissue surface and its characteristics were regulated by varying the matrix stiffness. Hydrogels are known to provide a convenient and structurally stable 3D microenvironment for cultured cells.[25,26] In general, even small changes in the 3D microenvironment, such as scaffold stiffness, can influence the behavioral expression of cells.[27,28] Therefore, regulating the stiffness of a hydrogel in the *in vitro* BBB mode is beneficial for simulating organs such as the brain.[1,29] At first, 3D BBB models were fabricated at different fibrinogen concentrations since increased fibrinogen concentration can increase the elastic modulus of fibrin gel.[30] In subsequent compression testing, we also demonstrated that there was a positive relationship between fibrinogen concentration and

elastic modulus. As expected, the obtained 3D BBB models with different fibrinogen concentrations had large phenotypic differences, but surprisingly these differed from previous reports in the literature. We originally thought the BMECs on a soft gel would more easily form a deeper hole structure as previous reports have shown that soft gel is more conducive to the migration of endothelial cells inside the model,[31,32] and the migration of BMECs into the model is the reason for hole formation. However, in our study, a shallow hole structure was generated on the softer 3D BBB model, and a deep hole structure was generated on the harder 3D BBB model. We have not found any similar cases in past reports. The size of the hole structure seemed to be random and was not changed significantly according to the 3D BBB model culture time and elastic modulus. We believe it is highly probable that BMECs show different gene expression on scaffolds of differing stiffness.

The formation of a capillary network within different 3D BBB models was also quantitatively analyzed. It is noteworthy that although the average capillary length at a low concentration was only about 15% higher than at a high concentration, the interval statistics showed that not only were more capillaries generated at a low concentration but also the ratio of long capillaries was much higher than in the high concentration model. Past reports have shown that increasing fibrinogen concentration results in higher fibril density and smaller pore size of the gel network, which makes it more difficult for BMECs to migrate and remodel the ECM in fibrin gels.[8] In addition, the transmission of factors that regulate cell adhesion and migration, such as the integrin, are also barriered by the fibrin gel networks.[33] Therefore, capillary formation is co-regulated by matrix elastic modulus, gel network size, and integrin transmission. Compression testing showed that the elastic modulus of the 3D BBB model was greater than the fibrin gel at a low concentration, but this was reversed at a high concentration. Combined with the results of hole structure and capillary network evaluation, we can speculate that for the low concentration model, a well-connected and dense capillary network will serve to enhance the model strength, and the capillaries can be considered as fibers. From a mechanical point of view, long fibers in the material will improve its mechanical properties.[34] Although many hole structures are generated on the model surface, they have only a small impact on the model construction due to their shallow depth. Therefore, the 3D BBB model

under low concentration conditions possesses a higher elastic modulus. On the other hand, in the high elastic modulus model, deeper hole structures may lead to model instability and collapse, while inside the model, the individual BMECs or short capillaries cannot enhance the model strength.[35] Therefore, the modulus of the 3D BBB model at high concentrations is lower than normal fibrin gel.

Next, the holes were evaluated with a low number of BMECs seeded on the model surface, which contributed to our explanation for the process of hole structure generation and the behavior pattern of BMECs. The results showed a clear relationship between the BMEC monolayer coverage and the BMEC seeding density. Basically, no hole structure was observed on the model with a low BMEC density, indicating that BMECs in this condition would first elongate and proliferate on the gel surface and not migrate to the inside of the gel. We think it is possible that when there are fewer BMECs, there is enough space on the model surface for their growth to a quantitative threshold, and they would not show the tendency of migration to the gel interior before reaching a point where they can completely cover the model.[36] When many BMECs were seeded, the limited space caused the BMECs to "crowd" each other, inducing their migration to the gel interior and finally forming the hole.

To verify the conjecture about the influence of BMEC migration behavior, the change of BMECs (2×10^5) on the model surface was later clarified by time-lapse experiments. The results shown in **Figure 2-6** for elastic modulus correspond to our earlier speculation based on the data shown in **Figure 2-3** and **Figure 2-4** about the relationship between modulus, capillary length, and hole depth. For the low elastic modulus 3D BBB model, the capillary length grows with increasing culture time, and therefore the intensity shows an increasing trend. For the high elastic modulus 3D BBB model, the hole also gradually forms with increasing culture time, and the collapse of the model structure causes a decrease in elastic modulus. On the first day of incubation, a "mountain" of aggregation could be observed on the model surface, and the BMECs still existed as undifferentiated pellets, indicating proliferation and competition among the BMECs. On the third day, the aggregation of BMECs ceased and they converged to form a monolayer, and the morphology changed to a flattened shape after differentiation, probably because BMECs which failed to obtain adhesion space fell off, and the successfully adhered

BMECs gradually formed a monolayer after differentiation.[36,37]

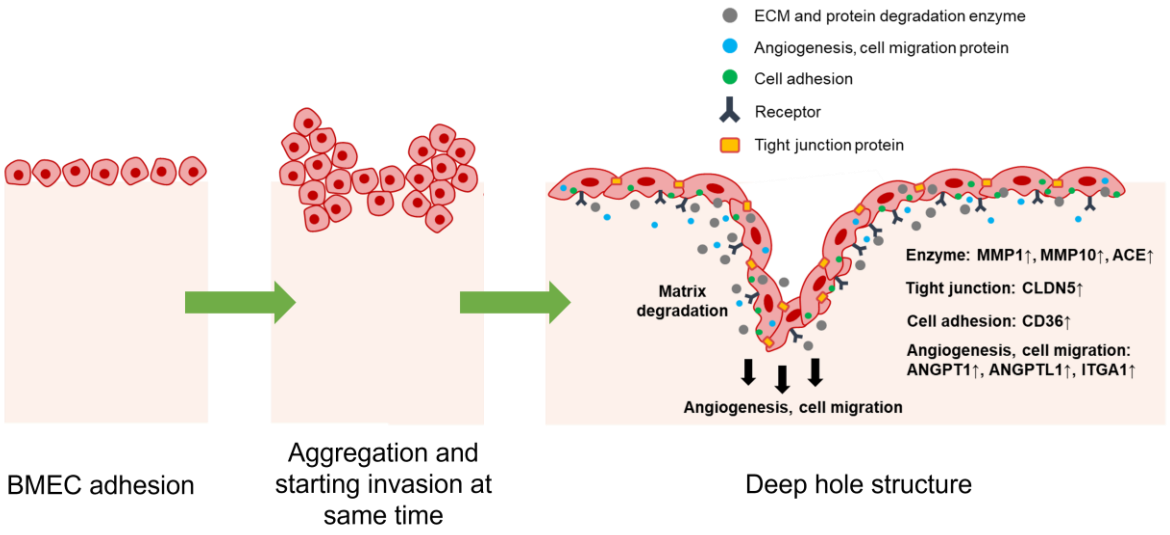

Figure 2-9. Schematic illustration of hole structure and capillary network formation in a 3D BBB model on a hard model surface.

We also evaluated the role and influence of supporting cells, namely ACs and PCs, in the hole structure formation process. Many studies have shown the existence of cell-cell interaction between ACs, PCs and BMECs, with positive significance for angiogenesis, tight junctions formation and expression of enzymatic systems.[38–40] We have labeled ACs and PCs respectively with CellTracker in our previous studies and demonstrated that ACs and PCs are in close proximity to the BMEC network in the tissue.[4,5] Hole structures were not formed on the model without ACs and BCs inside the gel, which demonstrated that ACs and PCs are important for inducing hole formation in the 3D BBB model.[6] Holes also formed on the model of only ACs and PCs inside and showed the same trend in that hole depth increased with increasing elastic modulus, indicating that the formation of holes occurred by BMEC behavior. Calculations showed that there were fewer holes than in the 3D BBB model with BMECs inside, indicating that hole formation is not limited to surface-to-inside processes, but that there are also BMECs growing from the inside and connecting to surface BMECs to form holes.

We next sought to perform RNA sequencing on the three types of models to understand the molecular processes involved in the hole formation and capillary network formation. In the analysis of GO enrichment terms for Hol compared to Net up-regulated genes, lysosome, ECM organization and proteolysis have high enrichment. This probably shows that cells in the models with a hole structure can more easily secrete factors that can dissolve fibrin and these

factors break down the scaffolds during the migration of BMECs. The GO enriched terms in Hol and Net showed substantial cell proliferation compared to BM, suggesting that ACs and PCs play a key regulatory role in BMEC proliferation. We also sought to clarify the mechanism of hole structure formation by analyzing key genes. We found there were no significant differences in transporter genes ABCB1, SLC2A1, and TFRC; tight junction gene TJP1; and endothelial marker PECAM1 (CD31). On the other hand, we found that the gene up-regulated in the Hol model may be related to the hole formation process depicted in **Figure 2-9**. Furthermore, MMP1 and MMP10 have already been shown to have effects on ECM degradation, and ACE is an enzyme gene related to proteolysis.[41,42] Although **Figure 2-8d** shows that the MMP1 and MMP10 genes in Hol were down-regulated compared to BM, CD31 marker showed that no hole structures appeared on BM. Therefore, MMP1, MMP10, and ACE genes may lead to the degradation of fibrin gel. Besides, ITGA1, CD36 are proteins involved in cell adhesion; ANGPT1, ANGPTL1, and COL21A1 are proteins involved in angiogenesis processes, so this may explain the simultaneous BMEC migration and hole formation.[43–46] CLDN5 is a gene encoding for Claudin-5, which is a protein related to the high density of the BMEC monolayer and the maintenance of BMEC barrier integrity.[47,48] Frizzled-1 encoded by the FZD1 gene, is a receptor of focal adhesion, collagen, and Wnt signaling pathway proteins.[49] These genes probably collectively guide the cell expression and induce the hole formation.

2.5 Conclusion

In this chapter, we regulated the hole and capillary network structure in an in vitro 3D BBB model with a special hole structure by adjusting the model elastic modulus. Specifically, we found the hole depth on the bottom surface increased with an increasing elastic modulus of the fibrin gel scaffold, and the internal capillary network length increased with decreasing elastic modulus. Through a series of experiments, we learned that when low numbers of BMECs are seeded on the model bottom surface, they will first perform proliferative behavior and not form holes. The process of hole formation in the 3D BBB model was clarified by time lapse experiments where we found that the BMECs first proliferate, leading to aggregation and

invasion when many BMECs are seeded on the model bottom surface, eventually forming a hole. Besides, by adjusting the cell composition in the 3D BBB model, we demonstrated that internal ACs and PCs are important for inducing hole formation on the model surface. From gene expression analysis, we found that the MMP1, MMP10 and ACE genes related to the process of ECM degradation and enzymatic systems, CLDN5 gene related to tight junctions, ANGPT1, ANGPTL1 gene related to angiogenesis, are up-regulated in models with a hole structure and are highly likely to influence the hole formation regulation process. However, there are still some issues in our study, such as we have not demonstrated the functional properties of the BBB model. In the future, we will perform model permeability testing and drug evaluation to improve the model. In conclusion, we demonstrated the possibility of establishing a regulated 3D BBB model and this may provide a new way to fabricate other complex capillary network models by modifying EC types such as human umbilical vein endothelial cells (HUVECs), human lymphatic endothelial cells (HLECs), and human pulmonary microvascular endothelial cells (HPMECs).

2.6 Reference

[1] A. Aazmi, H. Zhou, W. Lv, M. Yu, X. Xu, H. Yang, Y. S. Zhang, L. Ma, *iScience* **2022**, *25*, 104110.

[2] N. J. Abbott, *Cell Mol Neurobiol* **2005**, *25*, 5.

[3] M. Campisi, Y. Shin, T. Osaki, C. Hajal, V. Chiono, R. D. Kamm, *Biomaterials* **2018**, *180*, 117.

[4] A. Figarol, M. Piantino, T. Furihata, T. Satoh, S. Sugiura, T. Kanamori, M. Matsusaki, *Biochemical and Biophysical Research Communications* **2020**, *533*, 600.

[5] F. Agathe, N. Yasuhiro, S.-M. Yukari, F. Tomomi, S. Kaoru, M. Matsusaki, *Biomed. Mater.* **2021**, *16*, 015006.

[6] M. Piantino, D.-H. Kang, T. Furihata, N. Nakatani, K. Kitamura, Y. Shigemoto-Mogami, K. Sato, M. Matsusaki, *Materials Today Bio* **2022**, *15*, 100324.

[7] B. A. Juliar, M. T. Keating, Y. P. Kong, E. L. Botvinick, A. J. Putnam, *Biomaterials* **2018**, *162*, 99.

[8] N. Salam, S. Toumpaniari, P. Gentile, A. Marina Ferreira, K. Dalgarno, S. Partridge, *Materials* **2018**, *11*, 1781.

[9] M. Keating, M. Lim, Q. Hu, E. Botvinick, *Acta Biomaterialia* **2019**, *87*, 88.

[10] R. Ito, K. Umehara, S. Suzuki, K. Kitamura, K. Nunoya, Y. Yamaura, H. Imawaka, S. Izumi, N. Wakayama, T. Komori, N. Anzai, H. Akita, T. Furihata, *Mol. Pharmaceutics* **2019**, *16*, 4461.

[11] T. Furihata, R. Ito, A. Kamiichi, K. Saito, K. Chiba, *J. Neurochem.* **2016**, *136*, 92.
[12] K. Umehara, Y. Sun, S. Hiura, K. Hamada, M. Itoh, K. Kitamura, M. Oshima, A. Iwama, K. Saito, N. Anzai, K. Chiba, H. Akita, T. Furihata, *Mol Neurobiol* **2018**, *55*, 5993.
[13] T. Quach, M. Tippens, F. Szlam, R. Van Dyke, J. H. Levy, M. Csete, *Liver Transpl* **2004**, *10*, 123.
[14] J. Schindelin, I. Arganda-Carreras, E. Frise, V. Kaynig, M. Longair, T. Pietzsch, S. Preibisch, C. Rueden, S. Saalfeld, B. Schmid, J.-Y. Tinevez, D. J. White, V. Hartenstein, K. Eliceiri, P. Tomancak, A. Cardona, *Nat Methods* **2012**, *9*, 676.
[15] D. Torre, A. Lachmann, A. Ma'ayan, *Cell Systems* **2018**, *7*, 556.
[16] I. Inza, P. Larrañaga, R. Blanco, A. J. Cerrolaza, *Artificial Intelligence in Medicine* **2004**, *31*, 91.
[17] P. A. Mundra, J. C. Rajapakse, *Journal of Biomedical Informatics* **2016**, *59*, 31.
[18] C. M. Ghajar, X. Chen, J. W. Harris, V. Suresh, C. C. W. Hughes, N. L. Jeon, A. J. Putnam, S. C. George, *Biophysical Journal* **2008**, *94*, 1930.
[19] J. J. Moon, J. E. Saik, R. A. Poché, J. E. Leslie-Barbick, S.-H. Lee, A. A. Smith, M. E. Dickinson, J. L. West, *Biomaterials* **2010**, *31*, 3840.
[20] M. Vigen, J. Ceccarelli, A. J. Putnam, *Macromol. Biosci.* **2014**, *14*, 1368.
[21] A. Brown, H. He, E. Trumper, J. Valdez, P. Hammond, L. G. Griffith, *Biomaterials* **2020**, *243*, 119921.
[22] J. I. Alvarez, T. Katayama, A. Prat, *Glia* **2013**, *61*, 1939.
[23] F. De Smet, I. Segura, K. De Bock, P. J. Hohensinner, P. Carmeliet, *ATVB* **2009**, *29*, 639.
[24] S. Kim, H. Lee, M. Chung, N. L. Jeon, *Lab Chip* **2013**, *13*, 1489.
[25] M. W. Tibbitt, K. S. Anseth, *Biotechnol. Bioeng.* **2009**, *103*, 655.
[26] S. R. Caliari, J. A. Burdick, *Nat Methods* **2016**, *13*, 405.
[27] G. Charras, E. Sahai, *Nat Rev Mol Cell Biol* **2014**, *15*, 813.
[28] S. van Helvert, C. Storm, P. Friedl, *Nat Cell Biol* **2018**, *20*, 8.
[29] S. Budday, R. Nay, R. de Rooij, P. Steinmann, T. Wyrobek, T. C. Ovaert, E. Kuhl, *Journal of the Mechanical Behavior of Biomedical Materials* **2015**, *46*, 318.
[30] H. Duong, B. Wu, B. Tawil, *Tissue Engineering Part A* **2009**, *15*, 1865.
[31] T. Luo, B. Tan, L. Zhu, Y. Wang, J. Liao, *Front. Bioeng. Biotechnol.* **2022**, *10*, 817391.
[32] Y. Duan, X. Li, X. Zuo, T. Shen, S. Yu, L. Deng, C. Gao, *J. Mater. Chem. B* **2019**, *7*, 5478.
[33] M. Jiroušková, J. K. Jaiswal, B. S. Coller, *Blood* **2007**, *109*, 5260.
[34] Y. K. Kumar, D. D. S. Lohchab, *IARJSET* **2016**, *3*.
[35] N. Annabi, S. M. Mithieux, E. A. Boughton, A. J. Ruys, A. S. Weiss, F. Dehghani, *Biomaterials* **2009**, *30*, 4550.
[36] E. Montañez, *Angiogenesis* **2002**, *5*, 167.
[37] E. H. Nguyen, W. T. Daly, N. N. T. Le, M. Farnoodian, D. G. Belair, M. P. Schwartz, C. S. Lebakken, G. E. Ananiev, M. A. Saghiri, T. B. Knudsen, N. Sheibani, W. L. Murphy, *Nat Biomed Eng* **2017**, *1*, 0096.
[38] D. Bonkowski, V. Katyshev, R. D. Balabanov, A. Borisov, P. Dore-Duffy, *Fluids Barriers CNS* **2011**, *8*, 8.
[39] D. H. Jo, J. H. Kim, J.-I. Heo, J. H. Kim, C.-H. Cho, *Mol Cells* **2013**, *36*, 465.
[40] T. Zidarič, L. Gradišnik, T. Velnar, *Bosn J of Basic Med Sci* **2022**, DOI 10.17305/bjbms.2021.6943.

[41] V. Beldent, A. Michaud, L. Wei, M. T. Chauvet, P. Corvol, *Journal of Biological Chemistry* **1993**, *268*, 26428.
[42] W. B. Saunders, K. J. Bayless, G. E. Davis, *Journal of Cell Science* **2005**, *118*, 2325.
[43] K. C. Ehrlich, M. Lacey, M. Ehrlich, *Epigenomics* **2019**, *11*, 169.
[44] M.-Y. Chou, H.-C. Li, *Genomics* **2002**, *79*, 395.
[45] H. Y. Huh, S. K. Lo, L. M. Yesner, R. L. Silverstein, *Journal of Biological Chemistry* **1995**, *270*, 6267.
[46] D. Xu, T. Li, R. Wang, R. Mu, *Front. Med.* **2021**, *8*, 674523.
[47] K. J. Hewitt, R. Agarwal, P. J. Morin, *BMC Cancer* **2006**, *6*, 186.
[48] C. Greene, N. Hanley, M. Campbell, *Fluids Barriers CNS* **2019**, *16*, 3.
[49] C. Bonnet, A. Brahmbhatt, S. X. Deng, J. J. Zheng, *RSC Chem. Biol.* **2021**, *2*, 1144.

Chapter 3

Construction of enzyme digested holes on hydrogel surface inspired by cell migration behavior

3.1 Introduction

In the construction of 3D *in vitro* vascular models, fibrin gels are widely used as scaffold materials, which are components of the ECM and thus have a high biocompatibility.[1–3] In addition, the proliferation and migration behavior of endothelial cells deeply affects the formation of blood vessels in tissue engineering.[4,5] It has been reported that vascular construction can be modulated by the mechanical properties (e.g., elastic modulus) of the scaffold material, and it has been observed that vessels are easier to form in less cross-linked and softer gels, since endothelial cells are easier to deform and migrate more easily in such gels.[6–8] Among the influences on endothelial cell migration, the effect of matrix metalloproteinases (MMPs) has been widely studied. MMPs can be classified into six categories: collagenases, gelatinases, stromelysins, matrilysins, MMP membrane-type-MMPs, and other MMPs.[9] MMPs can digest the ECM components, leaving empty spaces allow migration of endothelial cells.[10–12] Therefore, MMPs have a regulatory function in the formation of a vasculature by endothelial cells. Inspired by this, it is possible to imagine the disintegration of scaffold structures by MMPs to fabricate hydrogels with opening hole

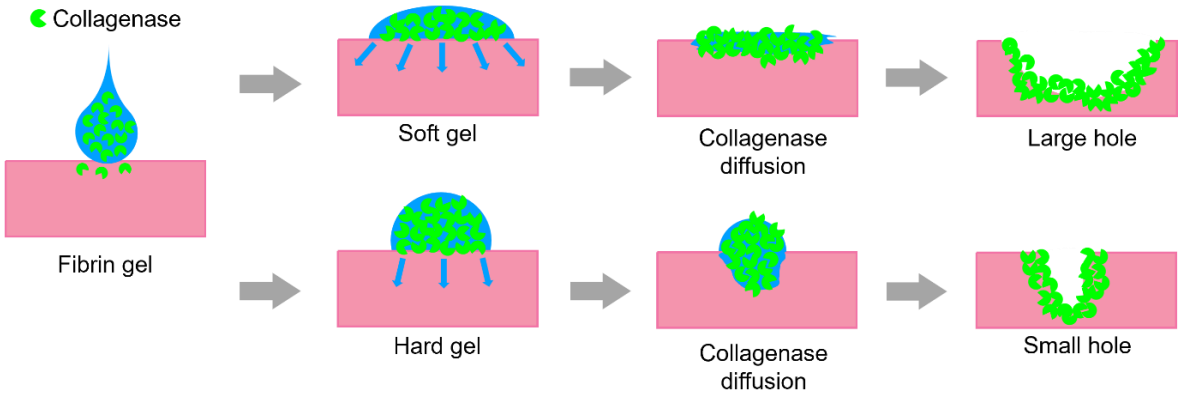

Figure 3-1 Schematic illustration of hole formation in fibrils gels of differing elastic moduli.

structures.

In chapter 2, we successfully obtained a perfusable *in vitro* blood-brain barrier (BBB) model with a capillary hole structure, using brain microvascular endothelial cells, pericytes, astrocytes and fibrin gel.[13–15] The hole structure in the model improves the efficiency of material exchange between the tissue interior and the external environment. Furthermore, we found that deeper capillary hole structures with smaller hole sizes were formed on hard fibrin gels. In contrast, shallower and larger hole structures were formed on soft fibrin gels. After gene expression assays, we found that endothelial cells secrete metalloproteinases that dissolve fibrin gels, which deeply affect the formation of hole structures. In this chapter, we developed a unique method of fabricating hydrogels with opening hole structures using a collagenase solution that mimics the MMPs secreted by endothelial cells, as shown in **Figure 3-1**. The effect of the volume and incubation time of the collagenase solution on the hole structure formation was also evaluated.

3.2 Experiments

3.2.1 Synthesis of FITC-labeled fibrinogen

First, 300 mg of fibrinogen (Ref. F8630-5G, Sigma Aldrich, St. Louis, MO, USA) was dissolved in 30 mL 0.1 M bicarbonate buffer (pH = 9, 0.1 M Na_2CO_3 : 0.1 M $NaHCO_3$ = 1 : 9) in a flask and the solution was stirred at 400 rpm. Then, 30mg fluorescein 5-isothiocyanate (isomer I) (FITC, Ref. 16151-66, Nacalai, ≥ 90.0% (HPLC), Kyoto, Japan) was dissolved in 1 mL dimethyl sulfoxide (DMSO, Ref. 043-07216, FUJIFILM Wako, Chemical Pure, Osaka, Japan) in an Eppendorf tube. The FITC solution was then added to the fibrinogen solution while stirring at 400 rpm at room temperature, then reacted in the dark for 1 h at room temperature. The crude product was transferred into a dialysis film (Mw: 12,000-15,000) after 1 h and dialyzed in bicarbonate buffer for 3 days during which the buffer was changed 3 times every day. The buffer was changed to ultrapure water on the final day. Finally, the samples were freeze-dried (Freeze Dryer FDU-2200, Eyela, Tokyo, Japan) for 3 days to obtain FITC-

fibrinogen sponge and kept in the dark before use.

3.2.2 Fabrication of fibrin gel models

First, a cylindrical mold was made with an 8 mm diameter biopsy punch (Ref. BP-80F, KAI INDUSTRIES CO. LTD., Gifu, Japan) on a 2 mm thick silicon rubber sheet (Ref. 6-611-004, AS ONE, Osaka, Japan). The rubber mold and the 24×24 mm size cover glass (Ref. C024241, Matsunami, Osaka, Japan) was surface plasma treated to prevent liquid leakage. Afterwards, the rubber mold was placed on the cover glass and pressed to ensure no gaps. For the fibrin gel model, fibrinogen solutions were prepared using Dulbecco's modified eagle medium (DMEM) without FBS/antibiotics dissolved at concentrations of 10, 50, and 100 mg/mL (with 1 wt% pre-synthesized FITC-fibrinogen) and 80 µl of each was transferred to Eppendorf tubes. Then, 0.4 U thrombin (Ref. T4648-10kU, Sigma Aldrich, St. Louis, MO, USA) was mixed in 40 µL of DMEM without FBS/antibiotics in another Eppendorf tube. The solutions from both Eppendorf tubes were quickly mixed before crosslink happened, then the inserts were incubated at room temperature for 20 min then 37 ℃ for 40 min to allow the fibrin gel to gelate. The final concentrations of fibrin gel were 7, 33, and 67 mg/mL.

3.2.3 Characterization of fibrin gel

Compression experiments were conducted to explore the mechanical behaviors under a 1 N loading cell by a 5 mm spherical indenter using an EZ-TEST instrument (Shimadzu, Kyoto, Japan) at a 1 mm/min loading speed for each concentration of fibrin gel. To eliminate any interference during the indention, only the stable range of 5-10% stress in the stress-strain curve was considered and further fitted into a linear slope. Young’s modulus of elasticity was automatically calculated by the instrument’s own software. The fibrin gels at each concentration were freeze-dried for three days and their swelling rates were obtained. Furthermore, collagenase (Type II, Ref. C6885-1G, Sigma Aldrich, St. Louis, MO, USA) solution with concentration of 2 wt% was prepared, then contact angle measurements were

performed on the surface of the fibrin gels with different concentrations using Drop Master (Kyowa Interface Science, Saitama, Japan).

3.2.4 Construction of the hole structure

Collagenase powder and rhodamine dextran powder (70 kDa, Ref. D1841, Sigma Aldrich, St. Louis, MO, USA) were dissolved in phosphate-buffered saline (PBS) solution to obtain a mixed solution with a concentration of 2 wt% collagenase and 0.1 wt% rhodamine dextran. The experiment comprised two groups according to the variables. In the first group, collagenase solution droplets with volumes of 2, 5 and 10 μL were dropped on the surface of the fibrin gels of different concentrations and incubated for 1 h at 37 ℃. In the second group, the volume of the collagenase solution droplets was fixed at 2 μl and the incubation time was varied to 30, 60 and 120 min, also at 37 ℃. After diffusion, all samples were washed three times with PBS solution.

3.2.5 Construction of a penetrating hole structure

To obtain a penetrating hole structure in the fibrin gel, additional cylindrical rubber molds with a diameter of 8 mm and a height of 6 mm were made. Fibrin gels with concentrations of 7 and 67 mg/mL were selected and and added to the molds. A 0.1 μL drop of 2 wt% collagenase solution was placed on the surface of the gel and incubated at 37 ℃ for 30 min and then removed. The fibrin gel liquid digested by collagenase was aspirated and new collagenase solution was added, and the above operations were repeated until the gel structure was penetrated.

3.2.6 Observation and quantification of the hole structure

All the above samples were observed by confocal laser scanning microscopy (CLSM)

(FluoView FV3000, Olympus, Tokyo, Japan). The images obtained were quantitatively processed and calculated using Imaris software (Oxford Instruments, Abingdon, UK) to obtain the volume of the hole structure. Specifically, the file was first opened in Imaris' 3D views and the following steps were followed: Surface, Source channel, Smooth, Threshold, Classify surfaces, Execute all creation and terminate the wizard, Statistics, All values, Volume. The volume obtained is the remaining volume of the gel after the collagenase digestion, and the collagenase digestion volume (hole volume) is obtained by subtracting this value from the original volume. The hole depth was calculated by ImageJ software.

3.2.7 Dextran diffusion test

The following 0.1 wt% solution was prepared: FITC, fluorescein isothiocyanate-dextran (4 kDa, Ref. 46944-100MG-F, Sigma Aldrich, St. Louis, MO, USA), fluorescein isothiocyanate-dextran (70 kDa, Ref. 46945-100MG-F, Sigma Aldrich, St. Louis, MO, USA), fluorescein isothiocyanate-dextran (250 kDa, Ref. FD250S-250MG, Sigma Aldrich, St. Louis, MO, USA), the solvent was PBS solution. The above prepared solution was dropped on the surface of the 67 mg/mL fibrin gel, incubated at 37 ℃ for 30 min, then washed with PBS solution three times and observed with CLSM.

3.2.8 Histology

The samples of fibrin gel after collagenase diffusion were fixed in 4% paraformaldehyde (PFA, Ref. 30525-89-4, Wako, Osaka, Japan). The samples were then sent to the Applied Medical Research Company for paraffin wax embedding and hematoxylin eosin staining. The histology was then observed using an FL Evos Auto microscope (Thermo Fisher, Waltham, USA).

3.2.9 Statistical analysis

All data are expressed as means ± SD. The values represent the means ± SD from three independent experiments, unless otherwise stated. Statistical comparisons between groups were analyzed using two-tailed Student's *t*-tests. A value < 0.05 was considered statistically significant. These are indicated in the graphs as $*p < 0.05$, $**p < 0.01$. *N.S.* denotes no significant difference.

3.3 Results and discussion

Fibrin gels with different mechanical properties were constructed, and this was achieved by varying the fibrinogen concentration. The elastic modulus of fibrin gels at different

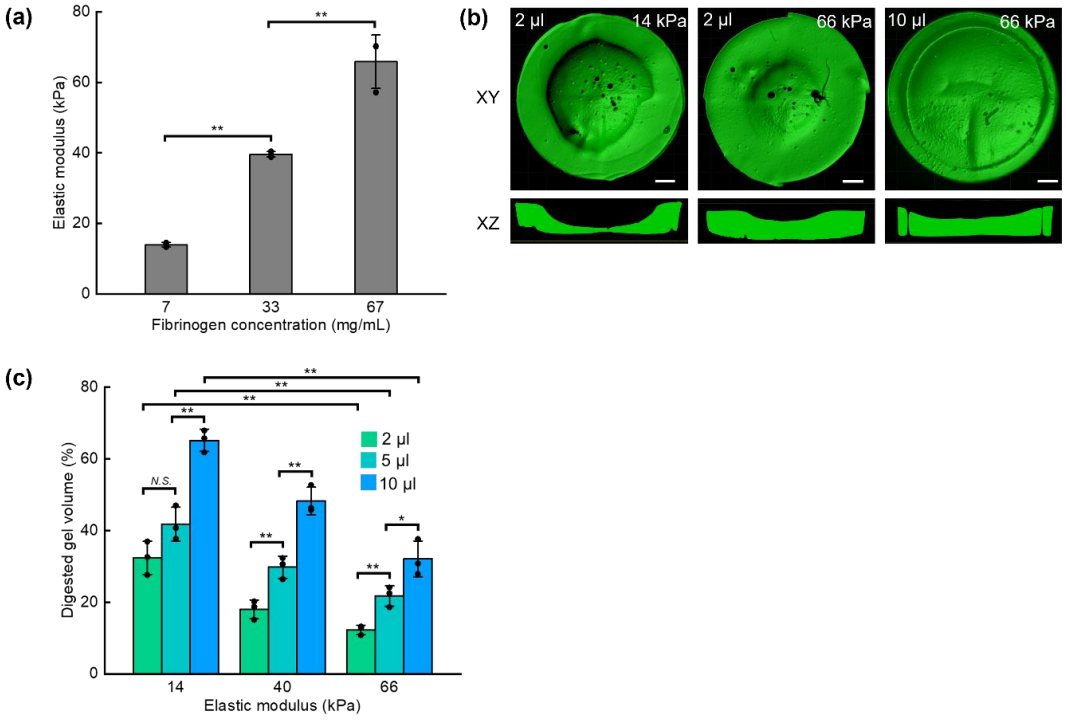

Figure 3-2 (a) Elastic modulus of fibrin gel with 7, 33, and 67 mg/mL fibrinogen concentration. (n=3) (b) 3D models from CLSM images of FITC-fibrin gel in different conditions. Collagenase drop volume 2 µL at 7 mg/mL of fibrinogen concentration, collagenase drop volume 2 µL at 67 mg/mL of fibrinogen concentration, and collagenase drop volume 10 µL at 67 mg/mL of fibrinogen concentration, after 1h of incubation. Scale bar: 1 mm (c) Calculated digested fibrin gel volume with 7, 33, and 67 mg/mL fibrinogen concentration after 1 h of incubation. (n=3). Data are presented as means ± S.D.

fibrinogen concentrations was then obtained by pressure testing, as shown in **Figure 3-2a**. Fibrinogen concentrations of 7, 33, and 67 mg/mL corresponded to elastic moduli of 14, 40, and 66 kPa, respectively. The mechanical strength of the fibrin gels increased with increasing fibrinogen concentration due to the increased cross-linking of the gels.[16] FITC fibrinogen was synthesized, which provides a fluorescent signal to allow observation of structural changes in the fibrin gel. **Figure 3-2b** shows a 3D model produced by Imaris software based on the FITC fluorescence images obtained by CLSM. Through the 3D model we could clearly observe that after dropping the same droplet volume of collagenase solution on fibrin gels of different stiffnesses, the size and depth of the hole structures formed

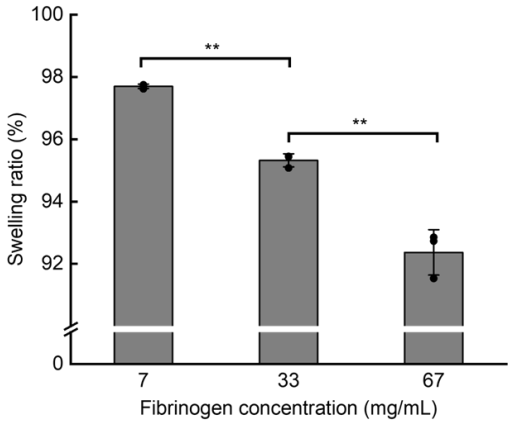

Figure 3-3 Swelling ratio of fibrin gel with different fibrinogen concentrations (n=3). Data are presented as means ± S.D.

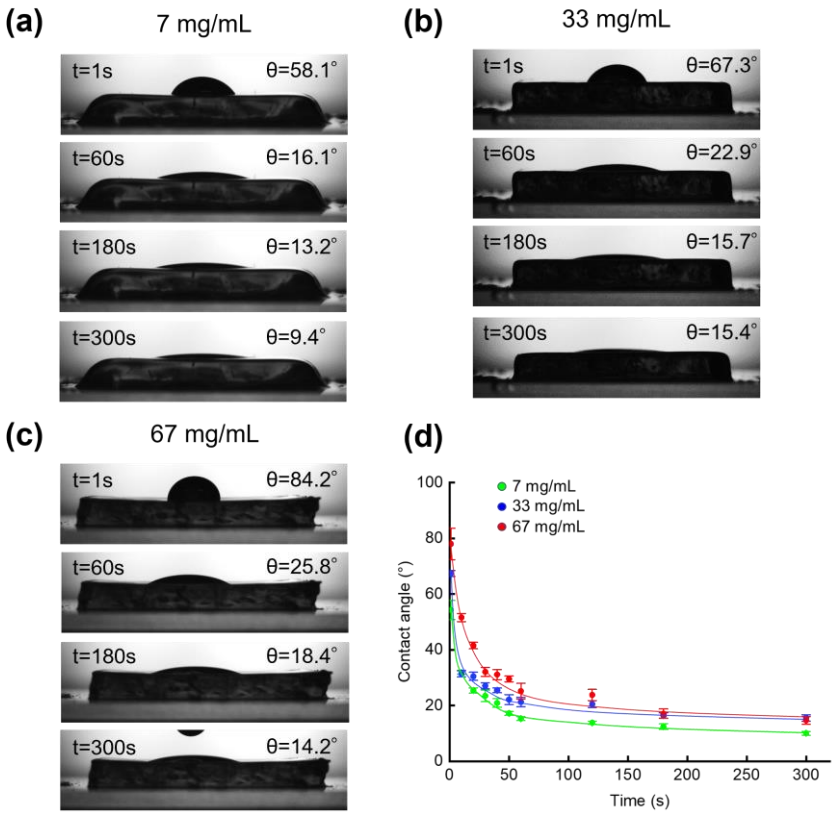

Figure 3-4 (a-c) Collagenase solution contact angles on different fibrinogen concentration (7, 33, 67 mg/mL) of fibrin gels. (d) The trend of contact angle with time for different fibrinogen concentrations (7, 33, 67 mg/mL) (n=3). Data are presented as means ± S.D.

on soft fibrin gels were significantly larger than those on hard fibrin gels, which can be attributed to the following two factors. First, soft fibrin gels are less cross-linked and have a higher water content as calculated by the swelling rate (**Figure 3-3**), thus making it easier for the collagenase molecules to diffuse. Second, the surface of soft fibrin gels is more hydrophilic, as calculated by the contact angle shown in **Figure 3-4**, so the surface area for the collagenase solution to diffuse on the fibrin gel surface is larger. For these two reasons, more of the soft fibrin gels are digested, resulting in larger and deeper hole structures. From the 3D model we could also observe that a higher volume collagenase solution digested more fibrin gel under the same stiffness of fibrin gel conditions. As shown in **Figure 3-2c**, the calculated results of hole volume are consistent with the observed results. At 14 kPa, 65.8% of the fibrin gel was digested by 10 µl of collagenase gel, which was clearly detrimental to the fabrication of hole structures. Therefore, we used 2 µl of collagenase solution in the subsequent experiments.

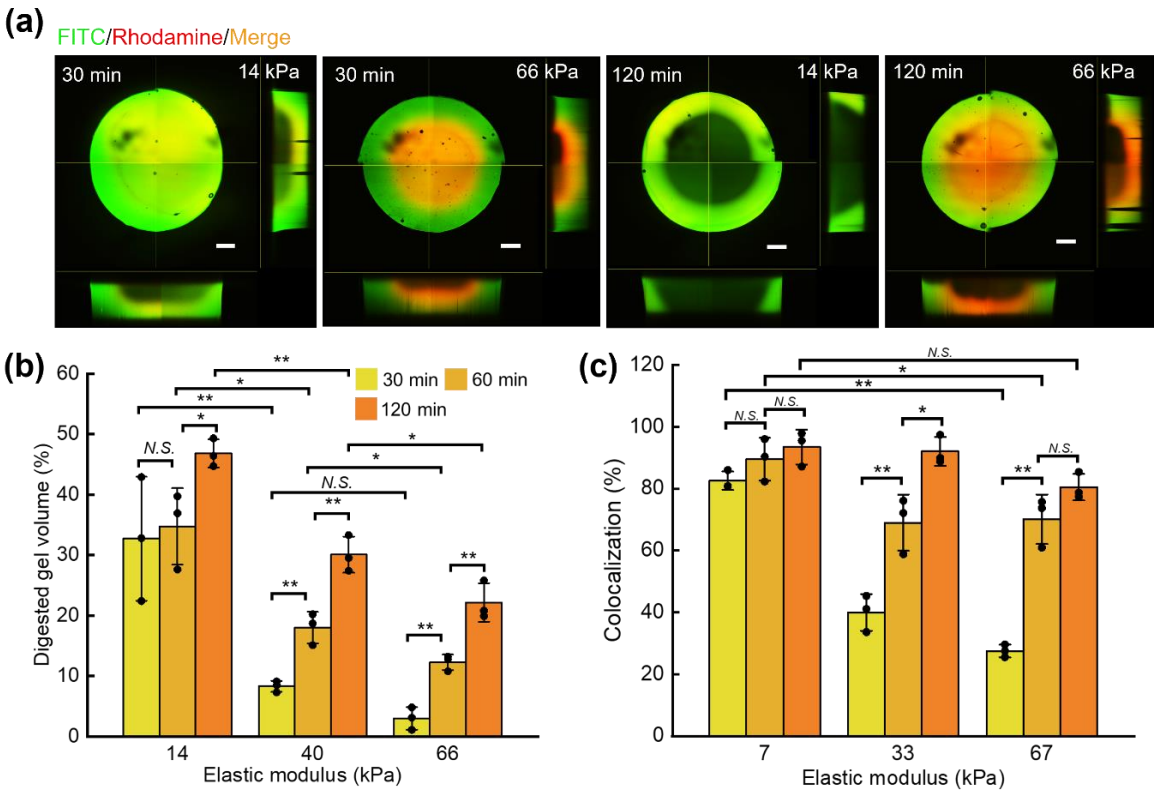

Figure 3-5 (a) CLSM images of FITC-fibrin gel with 2 µL collagenase drop volume in different conditions. Scale bar: 1 mm (b) Calculated digested fibrin gel volume with 2 µL collagenase drop volume at 7, 33, and 67 mg/ml fibrinogen concentration after 30, 60, 120 min of incubation. (n=3). (c) Calculation of rhodamine and FITC signal colocalization in fibrin gel (n=3). Data are presented as means ± S.D.

In the next experiments, we examined the effect of digestion time on fibrin gels. As shown in **Figure 3-5a**, these images were obtained by CLSM observation, and to observe the diffusion of collagenase we added rhodamine dextran showing a red signal to the collagenase solution. It can be seen from the CLSM images that, regardless of the hardness of the fibrin gel, the volume of the digested gel increased, and the depth gradually increased as the incubation time became longer (**Figure 3-6**). In addition, even though the depth of the hole in the hard fibrin gel increased after a longer digestion time, there was no notable change in the width of the hole structure formed. It was speculated that this is due to the difficulty for collagenase to diffuse in the hard gel, making it easier for collagenase to digest the fibrin gel in the vertical direction. The specific calculation results are shown in **Figure 3-5b**. After 30 min of incubation, only 3% of the gel was digested for a 66 kPa gel, while up to 32.7% of the gel was digested with 14 kPa,

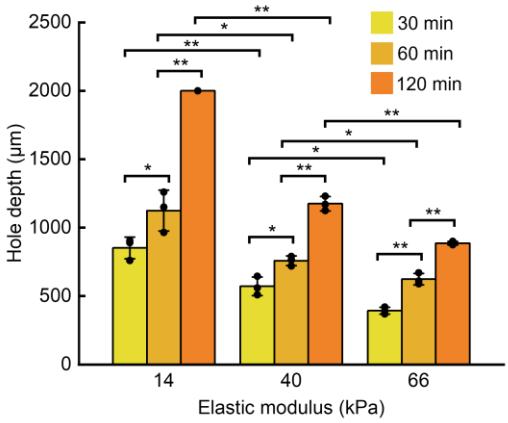

Figure 3-6 Hole depth of fibrin gel with different incubation times (n=3). Data are presented as means ± S.D.

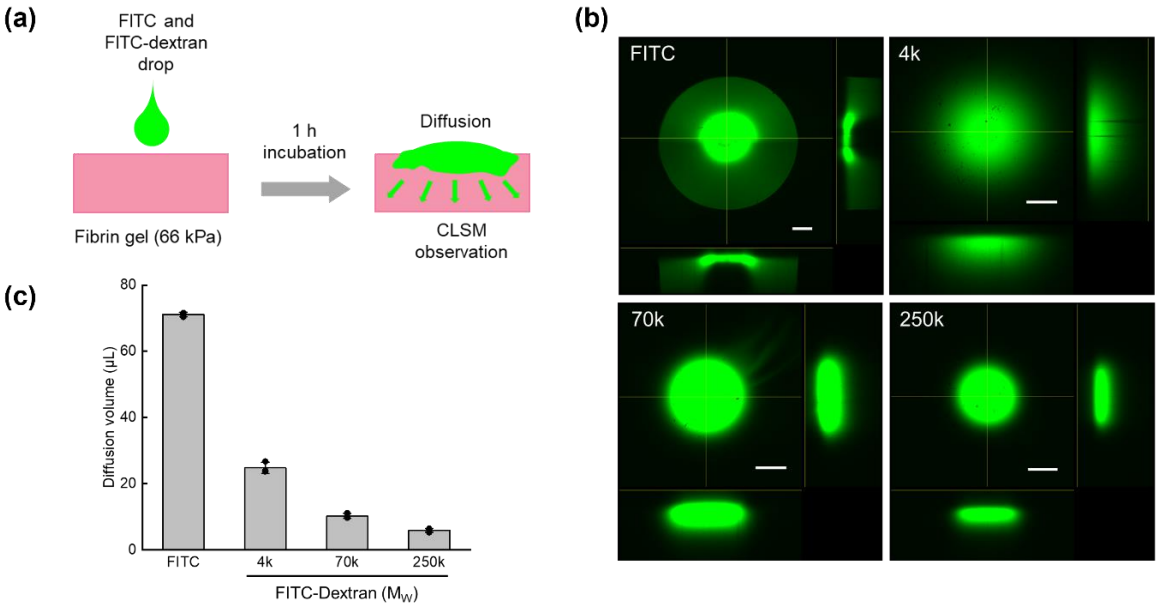

Figure 3-7 (a) Schematic illustration of FITC and FITC-dextran diffusing in hard fibrin gel. (b) CLSM images of FITC and FITC-dextran diffusion volume with different molecular weights (4k, 70k, 250k) in 66 kPa fibrin gel. Scale bar: 1 mm (b) Calculation of FITC-dextran diffusion volume in 66 kPa fibrin gel (n=3). Data are presented as means ± S.D.

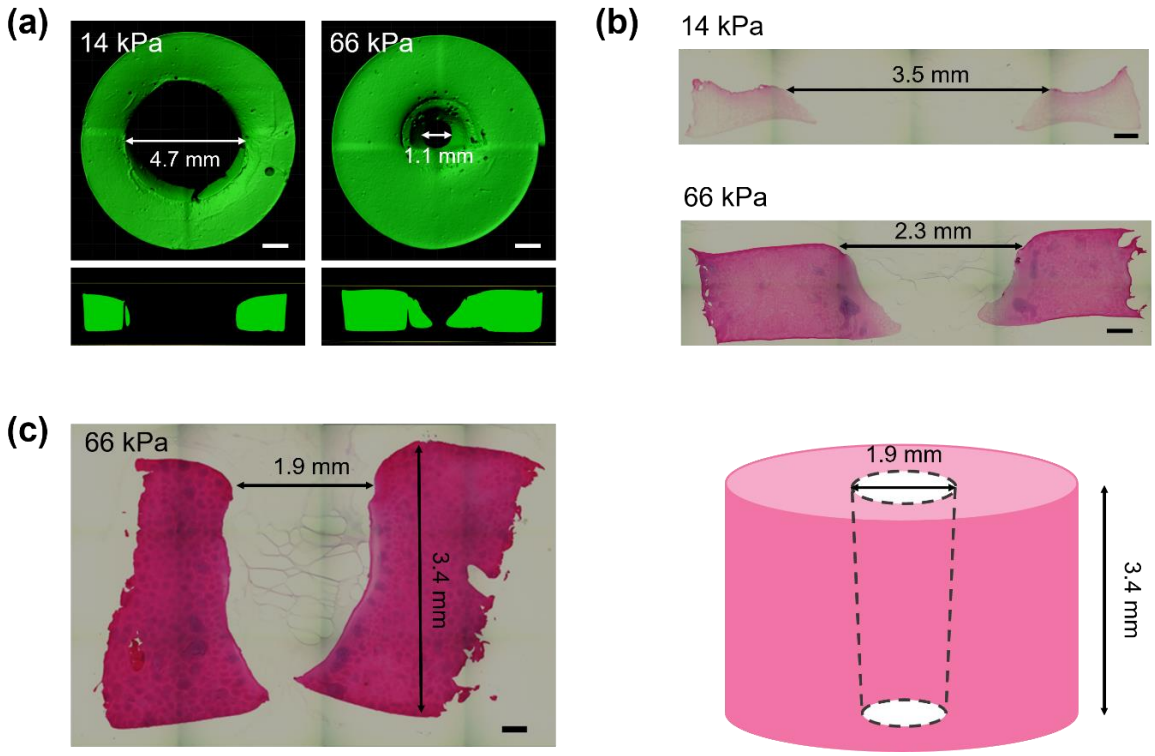

Figure 3-8 (a) 3D models from CLSM images of FITC-fibrin gel with a penetrating hole structure. Scale bar: 1 mm (b) Histology of FITC-fibrin gel with a penetrating hole structure. Scale bar: 300 μm (c) Histology of FITC-fibrin gel with a deep, penetrating hole structure. Scale bar: 300 μm

so it can be concluded that a harder fibrin gel should be selected if a smaller diameter hole structure is desired. This is consistent with the results obtained for hole structures formed by endothelial cell behavior. **Figure 3-5c** shows the co-localization calculations of the FITC signal for the rhodamine signal, and the calculations confirmed that collagenase had difficulty diffusing in the fibrin gel at 66 kPa. The molecular weight of collagenase was found to be 69-130 kDa. To simulate the diffusion of collagenase, FITC-dextran with different molecular weights was chosen and the solution was dropped on a fibrin gel at 66 kPa (**Figure 3-7a**). The CLSM images are shown in **Figure 3-7b**. As expected, we found that the low molecular weight FITC monomer diffused throughout the gel after 1 h incubation, and the area of diffusion became smaller as the molecular weight of FITC-dextran increased. After calculation (**Figure 3-7c**), the diffusion volume of 250 kDa FITC-dextran was only 1/10 of the FITC monomer, which is consistent with the result that collagenase does not diffuse easily on hard gels.

Finally, a penetrating hole structure was fabricated on the fibrin gel, as shown in **Figure 3-8a**. It was possible to fabricate hole structures with smaller diameters in hard fibrin gels, and

the diameter of the bottom hole on the 66 kPa gel was 1.1 mm, while the hole on the 14 kPa gel was 4.7 mm. The histology also shows that a penetrating hole structure was obtained (**Figure 3-8b**). Although the sample shrank, it was still found that the holes formed on the 66 kPa gel sample were smaller than those on the 14 kPa gel sample. This supports our hypothesis about the hole formation mechanism. **Figure 3-8c** shows the histology with a deeper penetrating hole structure fabricated on a 66 kPa fibrin gel. The structure demonstrates the feasibility of fabricating hydrogels with opening hole structures by collagenase dropping.

3.4 Conclusion

In this chapter, we were inspired by the migration behavior of endothelial cells and successfully used enzymes to fabricate opening hole structures on a hydrogel's surface. This method may provide a new way to fabricate 3D vascular opening models, and the future goal is to fabricate hole structures on the surface of fibrin gels with endothelial cells, and to culture and observe the tissues.

3.5 Reference

[1] S. D. Sackett, D. M. Tremmel, F. Ma, A. K. Feeney, R. M. Maguire, M. E. Brown, Y. Zhou, X. Li, C. O'Brien, L. Li, W. J. Burlingham, J. S. Odorico, *Sci Rep* **2018**, *8*, 10452.

[2] J. Nicolas, S. Magli, L. Rabbachin, S. Sampaolesi, F. Nicotra, L. Russo, *Biomacromolecules* **2020**, *21*, 1968.

[3] C. Schneider-Barthold, S. Baganz, M. Wilhelmi, T. Scheper, I. Pepelanova, *BioNanoMaterials* **2016**, *17*, 3.

[4] N. Gupta, J. R. Liu, B. Patel, D. E. Solomon, B. Vaidya, V. Gupta, *Bioengineering & Translational Medicine* **2016**, *1*, 63.

[5] A. K. Badekila, S. Kini, A. K. Jaiswal, *J Cell Physiol* **2021**, *236*, 741.

[6] M. Vigen, J. Ceccarelli, A. J. Putnam, *Macromol. Biosci.* **2014**, *14*, 1368.

[7] A. Brown, H. He, E. Trumper, J. Valdez, P. Hammond, L. G. Griffith, *Biomaterials* **2020**, *243*, 119921.

[8] K. Chwalek, M. V. Tsurkan, U. Freudenberg, C. Werner, *Sci Rep* **2014**, *4*, 4414.

[9] S. Quintero-Fabián, R. Arreola, E. Becerril-Villanueva, J. C. Torres-Romero, V. Arana-Argáez, J. Lara-Riegos, M. A. Ramírez-Camacho, M. E. Alvarez-Sánchez, *Front. Oncol.* **2019**, *9*, 1370.

[10] H. A. Fernandez, K. Kallenbach, G. Seghezzi, E. Grossi, S. Colvin, R. Schneider, P. Mignatti, A. Galloway, *Journal of Surgical Research* **1999**, *82*, 156.
[11] J. D. Raffetto, R. A. Khalil, *Biochemical Pharmacology* **2008**, *75*, 346.
[12] N. Hiraoka, E. Allen, I. J. Apel, M. R. Gyetko, S. J. Weiss, *Cell* **1998**, *95*, 365.
[13] F. Agathe, N. Yasuhiro, S.-M. Yukari, F. Tomomi, S. Kaoru, M. Matsusaki, *Biomed. Mater.* **2021**, *16*, 015006.
[14] M. Piantino, F. Louis, Y. Shigemoto-Mogami, K. Kitamura, K. Sato, T. Yamaguchi, K. Kawabata, S. Yamamoto, S. Iwasaki, H. Hirabayashi, M. Matsusaki, *Materials Today Bio* **2022**, *14*, 100232.
[15] M. Piantino, D.-H. Kang, T. Furihata, N. Nakatani, K. Kitamura, Y. Shigemoto-Mogami, K. Sato, M. Matsusaki, *Materials Today Bio* **2022**, *15*, 100324.
[16] R. I. Litvinov, J. W. Weisel, *Matrix Biology* **2017**, *60–61*, 110.

Concluding Remarks

In this thesis, the author described how to control the blood capillary network and hole structure formation by regulating elastic modulus of scaffolds.

In chapter 1, the author reported on the generation of 3D capillary tissue and how the adjustment of CMF amount, NHDF number and HUVEC number affects the blood capillary growth. In the case of a fixed cell number, since NHDF can secrete collagen as a cross-linking agent to enhance tissue strength, increasing the amount of CMF reduced the cell density of the tissue and decreased the mechanical strength of the 3D tissue. In the case of a fixed CMF amount, too large or too small of cells density were not conducive to the growth of capillaries in 3D tissues, and NHDF and HUVEC synergistically regulated the growth of capillaries.

In chapter 2, the author regulated the hole and capillary network structure in a 3D BBB *in vitro* model with a special hole structure by adjusting the model elastic modulus. Specifically, the author found the hole depth on the bottom surface increased with an increasing elastic modulus of the fibrin gel scaffold, and the internal capillary network length increased with decreasing elastic modulus. It demonstrated the possibility of establishing a regulated 3D BBB model and this may provide a new way to fabricate other complex capillary network models.

In Chapter 3, the author was inspired by the migration behavior of endothelial cells and successfully used enzymes to fabricate opening hole structures on the hydrogels surface. This method may provide a new way to fabricate 3D vascular opening models.

List of Publications

Chapter 1

1. Extracellular Matrix Density and Cell Number on Blood Capillary Formation in Three-Dimensional Tissue
   Yucheng Shang, Jinfeng Zeng, Zhengtian Xie, Naoko Sasaki, and Michiya Matsusaki.
   Bull. Chem. Soc. Jpn., **2022**, *95*, 1163-1168.

Chapter 2

2. Control of Blood Capillary Networks and Holes in Blood-Brain Barrier Models by Regulating Elastic Modulus of Scaffolds
   Yucheng Shang, Marie Piantino, Jinfeng Zeng, Fiona Louis, Zhengtian Xie, Tomomi Furihata, and Michiya Matsusaki.
   Materials Today Bio **2023**, *Accepted.*

Chapter 3

3. Construction of enzyme digested holes on hydrogel surface inspired by cell migration processes
   Yucheng Shang, Jinfeng Zeng, and Michiya Matsusaki.
   BBRC **2023**, *Accepted*.

Supplementary publications

1. Cancer Stem Cell Microenvironment Models with Biomaterial Scaffolds *In Vitro*.
   Ghmkin Hassan, Said M. Afify, Shiro Kitano, Akimasa Seno, Hiroko Ishii, **Yucheng Shang**, Michiya Matsusaki and Masaharu Seno.
   Processes, **2021**, *9*, 45.

2. Synthesis of phosphonate-containing mesoporous silica spheres under basic condition.
   Shota Yamada, **Yucheng Shang**, Iori Yamada, and Motohiro Tagaya
   Adv. Powder Technol., **2019**, *30*, 1116-1119.

Acknowledgments

This study was carried out from 2020 to 2023 at Department of Applied Chemistry, Graduate School of Engineering, Osaka University. In the past three years, I have received a lot of assistance and support for my study and daily life. Upon the completion of this thesis, I would like to express my gratitude to all those who have helped me.

First and foremost, I would like to express my sincere and deep gratitude my supervisor, Prof. Michiya Matsusaki for his invaluable advice, continuous support, earnest encouragement, and patience at every stage of the research project. His energy and passion for knowledge and education have had such a great influence on me, and I believe they will always be a beacon in my future career.

I am deeply grateful to the thesis committee: Prof. Toshiyuki Kida and Prof. Kazuya Kikuchi, who generously provided knowledge and expertise. Thanks to Prof. Tomomi Furihata in School of Pharmacy, Tokyo University of Pharmacy and Life Sciences (Hachioji, Tokyo) Japan for providing the three BBB cell lines (BMEC, AC, PC). Thanks to Ms. Zhang Huiting in AIST (Osaka University) for assisting me in using OCT and processing data analysis.

Besides my supervisor, I am also deeply grateful to Assistant Prof. Masahiko Nakamoto and Assistant Prof. Kenta Homma, and Specially Appointed Assistant Prof. Fiona Louis for their insightful comments and suggestions for my research. Thanks Dr. Dong-Hee Kang, Dr. Dr. Naoko Sasaki, Dr. Jinfeng Zeng, Dr. Zhengtian Xie, Dr. Piantino Marie Virginie, Dr. Muhammad Asri Abdul Sisak and for their comments, suggestions and guidance to my experiments.

I would like to offer my special thanks to Ms. Eri Enomoto and Ms. Chika Sugiki for their warmhearted support and kind help in the laboratory affairs and daily life.

My appreciation also goes to the previous and current fellows in the laboratory: Thanks to Visiting researcher Asuka Kato, Yoshihiro Kodama, Yuka Yoshinouchi, Mizuho Suzuki, Dr. Keisuke Sumiyoshi, and Dr. Quentin Muller. Thanks to Ms. Yukiko Sorayama, Mr. Hao Liu,

Ms. Jinyu Li, Mr. Kazuma Ishiguro, Mr. Noboru Hiraoka, Mr. Tomoyuki Suezawa, Mr. Daisuke Tomioka, Ms. Yuning Zhang, Ms. Lingyu Pei, Mr. Shogo Shimada, Mr. Ryo Mitsuyasu, Mr. Rei Miyata, Mr. Yuki Koba, Mr. Tomoya Matsuo, Mr. Kazuki Moroishi, Mr. Kazuki Yoshida, Mr. Tamaki Kumauchi, Ms. Skulya Bunuasunthon, Mr. Ryosuke Isobe, Mr. Yusuke Kajiura, Ms. Kaori Hayazaki, Mr. Rentaro Sakamoto, Ms. Chun-Yi Wu, Ms. Roko Akehi, Mr. Ryoto Itani, Mr. Kanta Iwamoto, Ms. Aya Nagura, Ms. Itsuki Miyaguni and so on. Thanks to their accompany and kind help for both research and daily life.

I would like to thank the Jisedai Program of the Japan Science and Technology Agency (JST) for providing me with financial support for research (JST SPING, JPMJSP2138) and financial support for living in Japan. And finally, I deeply thanks to my parents and friends who endured this long process with me, always offering support and love.

Finally, I am deeply grateful to my parents because they not only supported me financially, but also encouraged me during my difficult times and believed that I could overcome them. I am grateful to my friends who have helped me and given me comfort in my soul.

June 2023

SHANG YUCHENG